Measuring Clear-Air Vertical Motions From Space

Basile Poujol, Sandrine Bony

AGU ADVANCING EARTH AND SPACE SCIENCES

AGU Advances

RESEARCH ARTICLE
10.1029/2024AV001267

Measuring Clear-Air Vertical Motions From Space

Basile Poujol[1] and **Sandrine Bony**[1]

[1]LMD-IPSL, Sorbonne Université, École Normale Supérieure, CNRS, Paris, France

Peer Review The peer review history for this article is available as a PDF in the Supporting Information.

Key Points:

- Clear-sky vertical velocities in the mid-troposphere can be retrieved from geostationary satellites
- These new satellite retrievals reveal the ubiquity of gravity waves and equatorial waves in cloud-free regions of the tropics
- Strong subsidence is observed in the vicinity of organized convective systems

Supporting Information:

Supporting Information may be found in the online version of this article.

Correspondence to:

B. Poujol,
basile.poujol@lmd.ipsl.fr

Citation:

Poujol, B., & Bony, S. (2024). Measuring clear-air vertical motions from space. *AGU Advances*, *5*, e2024AV001267. https://doi.org/10.1029/2024AV001267

Received 10 APR 2024
Accepted 12 JUL 2024

Author Contributions:

Conceptualization: Basile Poujol, Sandrine Bony
Formal analysis: Basile Poujol, Sandrine Bony
Funding acquisition: Sandrine Bony
Methodology: Basile Poujol, Sandrine Bony
Software: Basile Poujol
Supervision: Sandrine Bony
Validation: Basile Poujol, Sandrine Bony
Visualization: Basile Poujol, Sandrine Bony
Writing – original draft: Basile Poujol
Writing – review & editing: Sandrine Bony

Abstract Measuring vertical velocity in the atmosphere has long been a challenge due to its small magnitude. Taking advantage of the modulation of free tropospheric relative humidity by vertical motions, we derive analytical relationships that allow us to retrieve vertical motions in clear air from geostationary measurements of brightness temperature in the infrared absorption band of water vapor. The new observations have a resolution of 1 hr and 2 km in time and space, respectively. They capture the variability of mesoscale and large-scale vertical velocity measured during field campaigns. In the mid-troposphere, clear-sky vertical motions are mostly subsiding but highly heterogeneous in space and time. Around organized deep convective systems, strong subsidence (>500 hPa·day^{-1}) is observed within a distance of a few hundred kilometers. In contrast, transient upward motions of up to 100 hPa·day^{-1} can occur at the mesoscale. Vertical motions in the clear-sky atmosphere appear to be primarily associated with buoyancy and gravity waves at the mesoscale, and with radiative cooling and equatorial waves at larger spatial scales. This new retrieval reveals a rich range of dynamical features that were previously invisible, thus shedding new light on tropical meteorology.

Plain Language Summary Vertical motions are a fundamental part of the general atmospheric circulation and play an important role in the distribution of clouds and water vapor at spatial scales varying from dozens to thousands of kilometers. However, they remain difficult to estimate due to their small magnitude. Here, new observations of vertical velocity are presented that are based on geostationary satellite images in the infrared domain, where water vapor is a strong greenhouse gas. By modulating humidity in the atmosphere, vertical motions indeed modulate the amount of infrared radiation emitted to space and measured by the satellite. The new observations have a high resolution in time and space, and are consistent with recent measurements from field studies. These observations show that clear-sky air is mostly moving downward, however, unlike previously thought, the air can also move upward in clear sky regions on short space and time scales. They also show strong downward motions around organized thunderstorms. Gravity waves (similar to waves in the ocean) appear to be the main cause for the observed vertical motions with a horizontal scale of about 100 km. These results reveal a rich range of dynamical features that were previously invisible, thus shedding new light on tropical meteorology.

1. Introduction

The state of the atmosphere and its evolution are best described by a self-consistent set of equations from fluid dynamics and thermodynamics that relates temperature T, water vapor content q, and the three wind components u, v and ω (Bjerknes, 1904). Among these five fundamental variables, vertical velocity is arguably the most difficult to measure, because it can be orders of magnitude smaller than its horizontal counterparts. Nevertheless, it can have substantial effects on the properties of the atmosphere at horizontal scales from few meters to thousands of kilometers. For example, synoptic vertical velocity is at the heart of the propagation of atmospheric perturbations such as mid-latitude anticyclones and depressions, but also tropical Kelvin and Rossby waves (Holton & Lindzen, 1968; Rossby, 1939). Although these waves are relatively well understood from a theoretical point of view, they have mostly been observed indirectly through their imprint on clouds, which is an incomplete view.

Atmospheric circulations are less understood, although believed to be crucial, at the so-called mesoscale (2–200 km; Orlanski (1975)). At this scale, the coupling between clouds, radiation, and circulation complicates our understanding of the organization of clouds and how they may evolve in a changing climate (Bony et al., 2015). In particular, the question of the key mechanisms responsible for the aggregation of deep convection is still largely open, despite the growing number of studies on this topic (Holloway et al., 2017; Wing et al., 2018). Dynamics in clear-sky areas are increasingly recognized as being key for convective aggregation (Bretherton et al., 2005; Emanuel et al., 2014; Wing & Emanuel, 2014). Indeed, theoretical and modeling studies have pointed out the

importance of processes such as gravity waves, shallow circulations, and radiative cooling (Muller et al., 2022), and observational studies have shown the influence of the dynamic environment in the triggering of convection (Hohenegger & Stevens, 2013). In addition, the magnitude of mid-tropospheric vertical velocity is key for controlling cloud type, cloud fraction (Bony & Dufresne, 2005), and the mesoscale organization of shallow and deep convection (Bellon & Coppin, 2022; Narenpitak et al., 2021; Schulz et al., 2021).

Therefore, a better knowledge of vertical motion in clear-sky areas of the tropical free troposphere would help understanding the coupling of atmospheric circulations with both deep and shallow convection. However, the measure of vertical velocity has been a long standing challenge (Bannon, 1949) and remains so. As a result, most observational studies still rely on reanalysis data to estimate tropospheric vertical motion in the tropics (e.g., Bony et al. (1997); Schulz and Stevens (2018), among many others), although the accuracy of reanalysis vertical velocities remains questionable and highly dependent on the situation (George et al., 2023; Huaman et al., 2022; Uma et al., 2021).

To alleviate this problem, various techniques were developed recently to measure vertical velocity at the mesoscale during field campaigns, using for example, the fall speed of radiosondes (Wang et al., 2009; Zhang et al., 2019) or latent heating measurements (Huaman et al., 2022). Among those methods, the most efficient way to measure mesoscale vertical velocity is probably the so-called kinematic method (Panofsky, 1946): a vertical profile of divergence can be converted into a vertical velocity profile using mass continuity. This concept has been used since decades to estimate vertical motions from synchronized networks of radiosondes and airborne platforms at the large scale, and later even at the mesoscale (Augstein et al., 1973; Fankhauser, 1969; Hardman et al., 1972; Lenschow et al., 1999; Nitta & Esbensen, 1974). More recently, Bony and Stevens (2019) have applied the kinematic method and estimated its accuracy, using dropsondes launched from an airplane flying circles. They have shown that precise estimates of area-averaged mesoscale vertical motion could be obtained, provided that the number of dropsondes used to compute the horizontal wind divergence was sufficient.

This method was used during recent field campaigns to produce observational data sets of mesoscale (∼200 km) vertical velocity in the tropical troposphere (George et al., 2021; Raymond & Fuchs-Stone, 2021). These unprecedented observations revealed the strong magnitude and fine vertical structure of vertical velocity in the free troposphere (Bony & Stevens, 2019), as well as the ubiquity of mesoscale circulations in the subtropical boundary layer (George et al., 2023). They also provided evidence for the transition from bottom-heavy to top-heavy deep circulations over the life cycle of convective systems in the Intertropical Convergence Zone (ITCZ) (Fuchs-Stone et al., 2020). Finally, they made it possible to refute the mixing-dessication hypothesis (Vogel et al., 2022), thus resolving a significant source of uncertainty in climate sensitivity. However, these advances also point out the value that vertical velocity observations at a high frequency and at the mesoscale would have for the our understanding of tropical meteorology and convective organization.

Here, we propose a method to retrieve vertical motion from geostationary satellite measurements. The underlying physical principle is depicted on Figure 1: vertical motions modulate the relative humidity of the atmosphere. This modulation has an impact on radiative transfer. Indeed, at wavelengths where water vapor is the dominant absorber, the level at which most photons reaching space are emitted (so-called emission level; Albrecht (1930)) is determined by the integrated column of water vapor above it. A subsiding motion will warm the atmosphere adiabatically while conserving specific humidity, thus decreasing relative humidity. The altitude of the emission level will decrease, and therefore the brightness temperature (that can be approximated as the atmospheric temperature at the emission level) will increase. Conversely, an ascending motion will have the opposite effect. In the absence of other modulating factors, brightness temperature variations in the water vapor absorption band are therefore primarily related to tropospheric vertical motion. This approach has been pioneered by Soden (1998), who showed that brightness temperature tendencies in the upper tropospheric water vapor channel could be related to large-scale subsidence and the associated radiative cooling in subtropical regions. It is the basis of the retrieval method that we propose to measure vertical motions from brightness temperature variations in the water vapor channel.

This article is structured as follows: in Section 2, we use recent theoretical advances in radiative transfer to derive a quantitative relationship between brightness temperature variations and vertical velocity. In Section 3, we implement this method using high rate geostationary satellite imagery. In Section 4, we discuss some striking features revealed by these new observations. We then evaluate the retrieval credibility and performance in a perfect model framework and against field campaign observations (Section 5). In Section 6, we investigate the

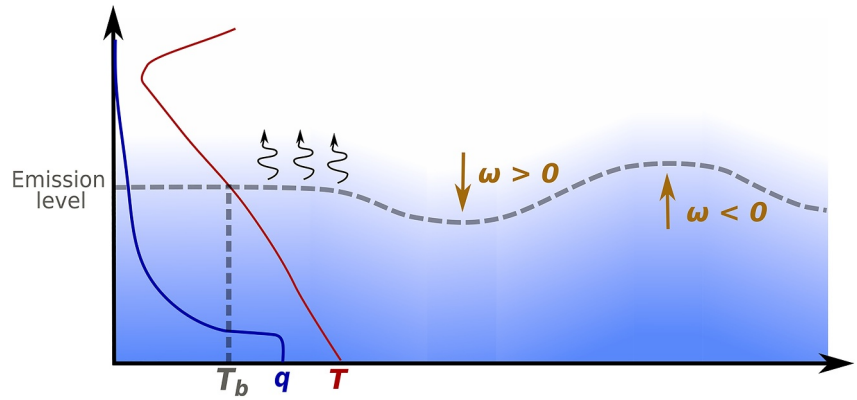

Figure 1. Schematic of the principle of the retrieval method. Vertical profiles of temperature T (red) and specific humidity q (blue curve and blue shading) are shown for a typical tropical atmosphere. Dashed gray lines indicate the position of the emission level height and of brightness temperature T_b. As shown on the right, vertical movements can modulate the humidity profile and thus the emission level height, causing variations in brightness temperature. Note that vertical displacement and moisture anomalies were drawn in phase on the schematic, which is not necessarily the case especially for gravity waves. This simplification is only present on the schematic, and such an assumption is not made in the rest of the study.

role of waves and radiation in controlling vertical velocity patterns observed from satellites. Finally, in Section 7, we summarize the results and discuss potential applications of the vertical motion retrievals for atmospheric sciences and beyond.

2. Theoretical Basis

The principle of the method is based on expliciting the relationship between brightness temperature variations and vertical velocity. It is done by using basic physical principles and radiative transfer theory. (A comprehensive derivation is provided in Supporting Information S1.) For convenience, all mathematical notations are summarized in a Table A1 in Appendix A.

We first derive two fundamental relationships (a) between temperature and relative humidity at the emission level, and (b) between vertical motion and relative humidity variations in the atmosphere. Then, we combine these two results to provide a quantitative link between brightness temperature variations and vertical velocity.

For this purpose, we make the following hypotheses or approximations:

- (H1) The atmospheric optical thickness τ_s at wavelength λ is such that $e^{-\tau_s} \ll 1$
- (H2) Relative humidity is locally vertically uniform in the emission layer (i.e., where the weighting function of the water vapor channel is nonzero, a layer thick only a few kilometers thick.)
- (H3) Water is considered to be the only significant absorber and the massic extinction coefficient κ at wavelength λ is proportional to pressure and independent on temperature (referred to as the pressure broadening approximation; Lorentz (1906); Kaplan (1952))
- (H4) The vertical temperature gradient is moist adiabatic (weak temperature gradient approximation; Charney (1963))
- (H5) Air is a perfect gas (Clapeyron, 1834), the effect of water vapor on density can be neglected.
- (H6) The hydrostatic approximation is valid (Pascal, 1664).
- (H7) Vertical turbulent fluxes of specific humidity are negligible in the free troposphere (supported by Couhert et al. (2010); see their Fig. 7d)
- (H8) Vertical velocity is locally vertically uniform within the emission layer

Note that in all this section, for the sake of simplicity, horizontal advection is neglected (wind is purely vertical). But the effect of horizontal advection will be accounted for in Section 3.

2.1. Link Between Relative Humidity and Brightness Temperature

Following Jeevanjee and Fueglistaler (2020b), the optical thickness τ at pressure p can be computed as:

$$\tau = \frac{\mu}{g}\int_0^p \kappa(p)q(p)\mathrm{d}p \tag{1}$$

where q is the water vapor mixing ratio, κ is the massic extinction coefficient, g is the gravity acceleration and $\mu = \sec(\theta)$ is a geometric factor function of the satellite zenithal angle θ.

Using (H2)-(H6) it is possible to estimate the value of this integral (the derivation is detailed in Text S1 of the Supporting Information S1), and then to relate relative humidity RH^* to air temperature T^* at the emission level $\tau = \tau^*$ through a function ϕ_κ such that:

$$RH^* = \phi_\kappa(T^*) = \frac{\Gamma_m R_d \tau^*}{\epsilon\kappa\mu}\frac{L_v/R_v + (\delta+1)T^*}{T^* e_{sat}(T^*)} \tag{2}$$

where δ is a dimensionless exponent such that locally $p \propto T^\delta$ with $\delta = \frac{g}{R_d\Gamma_m}$ (as shown in Supporting Information S1).

This relationship is very similar to the one derived by Soden and Bretherton (1993) who found that the fraction $RH\mu/\Gamma_m$ was proportional to $1/e_{sat}(T^*)$, although here some additional linear dependence on T^* is also present due to our slightly less strong assumptions. This kind of equation has long been used to retrieve upper tropospheric humidity products from passive infrared observations (Soden & Bretherton, 1993). Indeed, assuming that brightness temperature is more or less equal to air temperature at the emission level ($T_b \approx T^*$), this equation predicts that for a given relative humidity, brightness temperature is given and independent on the mean temperature of the atmosphere. This is known as the Simpson's law (Ingram, 2010; Jeevanjee et al., 2021) and it is this property that enables to determine relative humidity solely based on brightness temperature in one spectral channel.

2.2. Link Between Vertical Velocity and Relative Humidity Variations

We now assume that relative humidity variations in the atmosphere are primarily due to horizontal and vertical motion. Under this assumption, that will be discussed later, let us study the drying caused by subsidence (or conversely, the moistening caused by ascent) in the vicinity of the emission level. Conservation of specific humidity along the trajectory of a parcel moving at a vertical pressure velocity ω over a time dt can be written:

$$q(p, t + \mathrm{d}t) = q(p - \omega\mathrm{d}t, t) \tag{3}$$

Note that this equation uses (H7) as it neglects turbulent fluxes that could mix specific humidity vertically. From this equation we can derive (see Text S2 in Supporting Information S1):

$$\frac{\mathrm{d}RH}{\mathrm{d}t} = -\frac{RH}{t_\omega} \tag{4}$$

where t_ω is a characteristic drying or moistening time of the troposphere, that depends on vertical velocity, but also on the temperature profile followed by the air parcel during its vertical motion. To account for this dependency, we use the decomposition from Adames et al. (2021):

$$\omega = \omega_{WTG} + \omega_a \tag{5}$$

- The first term corresponds to the component of vertical velocity that satisfies the weak temperature gradient approximation, which is typically caused by persistent radiative cooling or diabatic heating anomalies. In this kind of motion, the temperature profile is externally constrained and the air parcel follows a moist adiabat. Then, the derivation yields:

$$\frac{1}{t_\omega} = \frac{\omega_{WTG}}{p}\left(\frac{L_v R_d \Gamma_m}{R_v g T} - 1\right) \tag{6}$$

- Conversely, the second component corresponds to deviations from the weak temperature gradient approximation (such as gravity waves and Kelvin waves). In those types of motion, air parcels follow a dry adiabat along their trajectory, which leads to:

$$\frac{1}{t_\omega} = \frac{\omega_a}{p}\left(\frac{L_v R_d}{R_v c_p T} - 1\right) \tag{7}$$

Beyond its usefulness for vertical motion retrievals, this relationship illuminates our understanding of radiation-circulation coupling. Indeed, radiative cooling can be an important driver of shallow circulations in the tropical atmosphere (Bretherton et al., 2005; Fildier et al., 2023; Muller & Held, 2012). This relationship shows that the characteristic drying time scale of the atmosphere associated with subsidence increases substantially with pressure and temperature. For a typical radiatively driven subsidence value of 2 hPa·hr^{-1}, t_ω varies from about 12 hr at 200 hPa to a week in the lower troposphere. Therefore, relatively weak subsidence can dry the upper troposphere on short time scales. This upper-tropospheric drying may then enhance radiative cooling rates and the associated shallow circulations in the lower troposphere (Fildier et al., 2023; Naumann et al., 2017), that play an important role in the organization of shallow and deep convection.

2.3. Link Between Vertical Velocity and Variations of Emission Temperature

Combining Equation 2 with Equations 4 and 7 leads to an analytical relationship between vertical velocity and air temperature variations at the emission level (see Text S2 in Supporting Information S1):

$$\omega = \frac{1}{k - \theta^*}\mathcal{F}(\theta^*, \delta, \psi) \times \frac{p}{T^*}\frac{\mathrm{d}T^*}{\mathrm{d}t} \tag{8}$$

where $\theta^* = R_v T^*/L_v$ is a dimensionless temperature at the emission level, $\psi = \theta^* \frac{\mathrm{d}\ln\Gamma_m}{\mathrm{d}\ln T}$ is a dimensionless measure of the temperature profile concavity, $k = 2/7$ and:

$$\mathcal{F}(\theta^*, \delta, \psi) = \frac{1 + (\delta + 2)\theta^*}{1 + (\delta + 1)\theta^*} + \delta\theta^* + \frac{\psi}{\delta + 1}\left(1 - \frac{\delta}{1 + \theta^*(\delta + 1)}\right) \tag{9}$$

This case corresponds to an adiabatic vertical motion, one of the two cases considered in Section 2.2. Using Equation 6 rather than 7 yields a similar result for the case of large-scale vertical motions that obey the weak temperature gradient approximation:

$$\omega = \frac{\delta}{1 - \delta\theta^*}\mathcal{F}(\theta^*, \delta, \psi) \times \frac{p}{T^*}\frac{\mathrm{d}T^*}{\mathrm{d}t} \tag{10}$$

The proportionality coefficient between vertical velocity and air temperature variations at the emission level depends on temperature and pressure, explicitly but also indirectly through the dimensionless parameters ψ, θ^* and δ. However, it does not depend on the spectroscopic extinction coefficient κ. This is remarkable as κ typically varies by orders of magnitude within the spectral width of a geostationary satellite channel. Thanks to this property, it is possible to spectrally integrate this equation without trouble, so that it can be used to retrieve vertical velocities even from broadband geostationary satellite channels. Moreover, as different channels sound different levels in the troposphere, this equation would make it possible to measure a vertical profile of vertical velocity using an ensemble of channels sounding different layers of the free troposphere.

3. Implementation of the Retrieval

3.1. Computation of Temperature at the Emission Level T^*

The equations derived above relate vertical velocity to time variations of air temperature at the emission level. Since the emission level is not an opaque black body, this temperature is not exactly brightness temperature, and its computation is the first step of the implementation.

To this end, we use the radiative transfer equation, which provides the radiance B_{sat} observed from space as an integral of the Planck function $B_\lambda(T)$ with respect to optical thickness τ:

$$B_{sat} = \int_0^{\tau_s} B(\tau) e^{-\tau} \mathrm{d}\tau + B_\lambda(T_s)\, e^{-\tau_s} \tag{11}$$

where the surface (or cloud-top) temperature T_s can be measured in the atmospheric window (10.4 microns channel), and τ_s is the atmospheric optical thickness at surface or cloud top at the considered wavelength.

An approximate inversion of this equation, detailed in Texts S2.1 and S2.2 of the Supporting Information S1 and inspired from the work of Jeevanjee and Fueglistaler (2020a), enables us to infer the air temperature T^* at the emission level ($\tau = \tau^*$) solely based on brightness temperature measurements in the water vapor channel and in the atmospheric window, as well as on the value of optical thickness τ^* at the emission level.

A simple hypothesis for the height of the emission level could be $\tau^* = 1$, as discussed in Jeevanjee and Fueglistaler (2020a). However, a computation reported in Text S2.3 of the Supporting Information S1 shows that temperature variations (unlike the absolute value of temperature) are on average observed at a lower level τ^*, which is given by:

$$\tau^* = 1 + \frac{hcR_v}{L_v \lambda k_B} = 1 + \frac{\mathcal{E}_{\text{photon}}}{\mathcal{E}_{\text{vap}}} \tag{12}$$

where $\mathcal{E}_{photon} = hc/\lambda$ is the energy of a photon at wavelength λ and $\mathcal{E}_{vap} = L_v k_B / R_v$ is the energy necessary to evaporate one molecule of water. Usually $\tau^* \approx 1.3$ but this quantity depends on wavelength. Fundamentally, the reason why the brightness temperature absolute value (observed around $\tau = 1$; Jeevanjee and Fueglistaler (2020a)) and brightness temperature variations are not observed at the same level from space is due to the non linearity of the Planck function with respect to optical thickness and temperature. Indeed, temperature is higher in the lower troposphere, therefore the Planck function is more sensitive to temperature increases there. Thus, for a similar increase ΔT in air temperature, the brightness temperature will increase more if the increase occurs in the lower part of the atmosphere. Interestingly, the deviation from the $\tau^* = 1$ law provided by computations corresponds to the ratio between the energy of a photon and the vaporization energy of a molecule of water vapor, but we do not have any satisfactory physical interpretation for that.

The first step of the implementation therefore consists in computing air temperature T^* at the level τ^* from brightness temperatures in the water vapor channel and in the atmospheric window, using the approximate inversion of the radiative transfer equation developed in Text S2 of the Supporting Information S1. Although T^* and brightness temperature T_b are generally considered as similar quantities, this computation refines the estimation of T^* by correcting the measured brightness temperature from the surface or cloud top emission and from non linear radiative transfer effects. This is performed for every geostationary satellite image.

3.2. Correction From Horizontal Advection

The next step of the implementation is to infer temporal variations of T^* from high-rate geostationary satellite images. Up to this point, horizontal advection has been neglected. However, horizontal wind at the emission level can cause brightness temperature variations due to advection, and the time derivative present in the equations derived in the theoretical part is a Lagrangian derivative. It is, at this point, difficult to know whether the effect of horizontal advection is significant. Therefore, we account for this effect, and will evaluate its magnitude a posteriori.

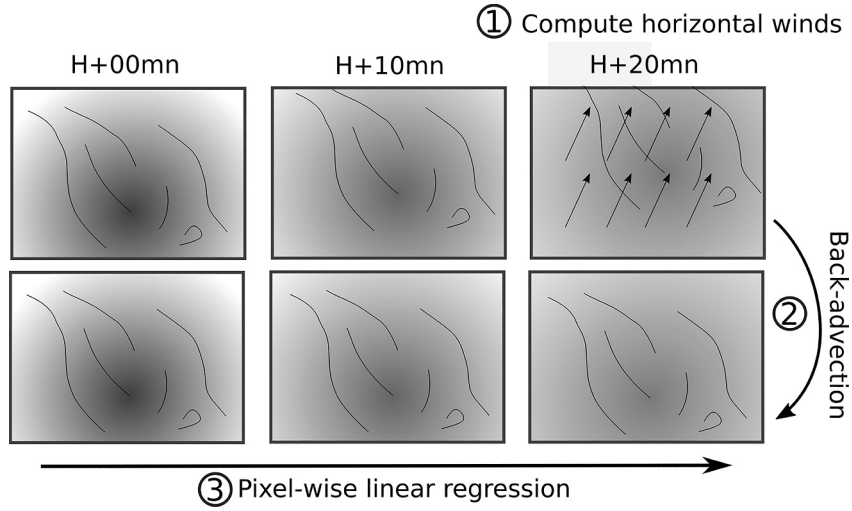

Figure 2. Computation of the Lagrangian derivative of temperature at the emission level. Black lines represent small-scale water vapor structures, whereas the background represents the mesoscale and large scale water vapor field. Step 1: horizontal winds are computed using a cross-correlation technique. Step 2: images of T^* (first row) are advected back onto their initial position using the computed winds (second row). Step 3: A pixel-wise linear regression provides the Lagrangian derivative $\mathrm{d}T^*/\mathrm{d}t$.

To compute this derivative, horizontal winds at the emission level are determined through cross-correlation. This technique is widely used in experimental fluid mechanics and in the production of atmospheric motion vectors (Forsythe, 2007). This is done in practice by filtering out gravity waves from the brightness temperature images through high pass and a rejection band spatial filters, and then using the OpenPIV Python library (Liberzon et al., 2021). The method provides an estimate of the horizontal wind $\vec{u}$ and its uncertainty $\Delta\vec{u}$ and has been validated against dropsonde data. Technical details on how this method is applied and validated are presented in Text S3 of the Supporting Information S1.

Once the horizontal wind has been determined, an hourly estimate of $\mathrm{d}T^*/\mathrm{d}t$ is performed as represented on Figure 2: all images taken between times t and $t + 1$ hr are selected and T^* is computed for each of them, as explained in the previous subsection (upper row of the figure). Then, the horizontal wind $\vec{u}$ determined by cross-correlation is used to advect back images onto their position at t, using a second order semi-Lagrangian advection scheme with bilinear interpolation. This step corrects images for advection (lower row of the figure). Finally, a pixel-wise linear regression of T^* as a function of t is performed, which directly provides the derivative $\mathrm{d}T^*/\mathrm{d}t$ as well as an uncertainty associated with the non linearity of points, noted Δ_{regr}.

3.3. Estimate of Vertical Velocity

Vertical velocity is then estimated from Equations 8 and 10. However, this requires a decomposition between vertical motions that satisfy the weak temperature gradient approximation, and deviations from it. We assume that the large scale component obeys the weak temperature gradient approximation, while the mesoscale and small-scale components correspond to adiabatic vertical motions. Note that, as shown by Adames (2022), this assumption is a simplification. Indeed, the separation between these two components of vertical motion is actually dependent on both the spatial and temporal scale of weather systems, and few large-scale weather systems, such as Kelvin waves, are expected to be adiabatic. A proper separation between vertical motions satisfying the weak temperature gradient approximation, and those deviating from it, would require advanced spectral analysis on the vertical motion features, that would be computationally too expensive to be applied on the large amount of data produced by geostationary satellites.

We decompose the estimation of $\mathrm{d}T^*/\mathrm{d}t$ into its large scale and small scale components as follows:

$$\frac{\mathrm{d}T^*}{\mathrm{d}t} = \left.\frac{\mathrm{d}T^*}{\mathrm{d}t}\right|_{small} + \left.\frac{\mathrm{d}T^*}{\mathrm{d}t}\right|_{large} \tag{13}$$

where the large scale component is estimated through a spatial convolution with a Gaussian kernel $\mathcal{G}(\sigma)$ of half width $\sigma = 1{,}000$ km:

$$\left.\frac{\mathrm{d}T^*}{\mathrm{d}t}\right|_{large} = \mathcal{G}(\sigma) * \frac{\mathrm{d}T^*}{\mathrm{d}t} \tag{14}$$

and the small scale term is computed as the residual using Equation 13.

Using this assumption, the two components $\left.\frac{\mathrm{d}T^*}{\mathrm{d}t}\right|_{small}$ and $\left.\frac{\mathrm{d}T^*}{\mathrm{d}t}\right|_{large}$ are ingested in Equations 8 and 10, respectively, to infer the corresponding vertical velocities ω_a and ω_{WTG}, that are finally added up to provide the final estimate of vertical motion over a 1-hr timestep (Equation 5).

Note that the use of Equations 8 and 10 requires pressure at the emission level (directly and through the parameters ψ and δ). Pressure is evaluated by interpolation knowing a temperature profile $T(p)$ and the temperature T^*. Since the vertical velocity estimate is only weakly dependent on pressure, p does not need to be estimated very precisely. Therefore, a simple tropical temperature profile is used, that is constructed by integrating a moist adiabat from the surface, assumed to be at 298K. Using observed temperature profiles instead of this idealized profile did not affect the results significantly.

Also, a correction term $-\omega_{SW}$ should be added to account for the effect of the absorption of shortwave radiation by water vapor. Indeed, this absorption modulates atmospheric temperature on the large scale. At fixed specific humidity, this temperature change causes relative humidity variations that are not linked to any vertical motion, and requires the introduction of a correction term. This effect is a typical example in which the hypothesis that relative humidity variations are only due to horizontal advection and vertical motion is broken. Details on the computation of this term are included in Text S4 of the Supporting Information S1. The magnitude of the correction is typically of 1–2 hPa·hr^{-1} at zenith.

In a last step, clouds and mountains are detected as regions where brightness temperature in the water vapor channel and in the infrared window channel differ by less than 10 K (i.e., where (H1) is not valid anymore). Additionally, semi-transparent clouds are detected using the difference between the so-called *clean* and *dirty* infrared window channels (around 10.5 and 11.5 μm, respectively) following Inoue (1985). Because the exact channel wavelength depends on the satellite, the threshold needed to be adapted by visual inspection and was set to 3.5 K for all Meteosat satellites and 2.5 K for all GOES and Himawari satellites. Vertical velocity measurements are discarded within 12 px (∼30 km) of these clouds. In addition, vertical velocity values exceeding a magnitude of 100 hPa·hr^{-1} are also discarded. These thresholds have been selected by visual inspection and usually correspond to artifacts due to clouds that were not detected by the cloud mask.

3.4. Time Sampling, Instrument Precision, and Limitations

The retrieval method described above translates a brightness temperature variation into a vertical displacement of air parcels, and, thereby, an estimate of mean vertical velocity over a given time interval. The question now arises of how the time interval should be selected in order to ensure a precise enough measurement of vertical motion.

The prefactor in Equation 8 varies, depending on atmospheric humidity and on the satellite channel, between 6 and 16 hPa·K^{-1}. Therefore, a brightness temperature change of 1K will typically correspond to a vertical motion of about 10 hPa over an hour. Moreover, it is known that the precision of geostationary satellite radiometers (in terms of time variability) is about 0.1 K (Yu et al., 2021). Vertical motions will therefore only be detected if they cause a brightness temperature change larger than this value. Therefore, to detect radiatively driven vertical motions, that are expected to be of the order of 1 hPa·hr^{-1}, vertical motions have to be estimated on an hourly timestep. In the remainder of this article, except if explicitly mentioned, we only use estimates of hourly vertical motion.

Given the high frequency of geostationary satellite observations, it is actually possible to compute vertical motions over shorter time periods. However, this comes at the price of a degraded precision. In particular, subhourly vertical velocity estimates can be performed, but are not expected to be accurate enough for detecting radiatively driven circulations. Therefore, the choice of the time interval over which $\mathrm{d}T_b/\mathrm{d}t$ is estimated depends

on the application: an interval of 1 hr seems appropriate for large-scale and radiatively driven vertical motions, while a 10 min interval will be more appropriate to study high-frequency gravity wave activity.

We still take advantage of the high-frequency observations by estimating vertical velocity not as a single difference between two brightness temperatures, but rather by performing a linear regression in time using all observations over a one-hour interval. While the advantage of using a linear regression compared to a simple one-hour difference was found to be small in terms of accuracy (not shown), using a linear regression enables the method to be much more robust to observational noise.

3.5. Uncertainty Quantification

The estimate of vertical velocity is associated with an uncertainty that mainly arises from two factors:

- The cross-correlation method used to derive horizontal winds (uncertainty $\Delta\vec{u}$)
- The linear regression providing the time derivative of brightness temperature (uncertainty Δ_{regr}).

To estimate the contribution of advection to dT^*/dt, a pixel-wise linear regression is performed on the difference between images of T^* before and after the backward advection step (first row minus second row of Figure 2). This provides an estimation of $\Delta_{adv} = dT^*/dt - \partial T^*/\partial t$, that is, of the advective contribution $\vec{u} \cdot \vec{\nabla} T^*$ to the Lagrangian derivative of T^*. The relative error on horizontal wind is then assumed to be equal to the relative error on this contribution. Assuming that the two sources of error discussed above are independent, the final uncertainty on ω is computed as:

$$\Delta\omega = \frac{1}{k-\theta^*}\mathcal{F}(\theta^*, \delta, \psi) \times \frac{p}{T^*}\sqrt{{\Delta_{regr}}^2 + \frac{\Delta\vec{u}^2}{\vec{u}^2}{\Delta_{adv}}^2} \tag{15}$$

Note that because of the nonlinearity of the error quantification equation, it is not possible to apply the scale separation technique presented above. The adiabatic equation was used because we are mainly interested in mesoscale motions, that are expected to mostly fall into the adiabatic category.

These analytical developments demonstrate that it is now possible to infer hourly vertical motions and their uncertainty at the kilometer-scale only using high-precision brightness temperature measurements in the water vapor and infrared window channels of geostationary satellites.

4. Vertical Velocities Measured From Space

By applying this methodology to geostationary satellite data, we now estimate vertical velocity over the whole tropics at a resolution of about 3 km. We investigate below the first outcomes of this retrieval and discuss them in the light of our current understanding of the dominant mechanisms responsible for cloud-circulation coupling.

Vertical motions have been retrieved for one year of data (2019) from GOES-16 (Schmit et al., 2017), Meteosat-8, Meteosat-11 (Schmetz et al., 2002) and Himawari-8 (Bessho et al., 2016) geostationary satellites. The method was applied to the 7.3 μm channel, which probes the mid- to lower free troposphere (from 600 hPa in dry conditions to 400 hPa in the ITCZ). Images were available with a temporal resolution of 20 mn for Himawari, 15 mn for Meteosat satellites and GOES-16 until March 2019, and 10 mn for GOES-16 from April 2019. Note that Himawari data were missing from August to October.

Figure 3 shows the retrieval result for 3 June 2019 at noon. Vertical velocity could be retrieved over most of the tropics, except in regions of deep convection or over the Andes, where the cloud top or the surface are too close to the emission level and (H1) is not valid, and where the water vapor field was spatially too homogeneous to estimate the horizontal wind through cross-correlation (Section 3.2). The different satellites agree well in regions where they overlap, except for Austral Africa where patterns are similar but there is a deviation in the mean value (we do not have a clear explanation for that discrepancy).

Observations reveal the presence of ubiquitous patterns of mid-tropospheric vertical motion from the kilometer-scale to the synoptic scale. Although vertical motions in the clear sky atmosphere are mostly subsiding, we also note areas of ascending motion with values that can reach -10 hPa·hr^{-1}. The size of these structures ranges from dozens (panel b) to a thousand of kilometers (panel c). Hovmöller diagrams and spectral analysis revealed that the

10.1029/2024AV001267

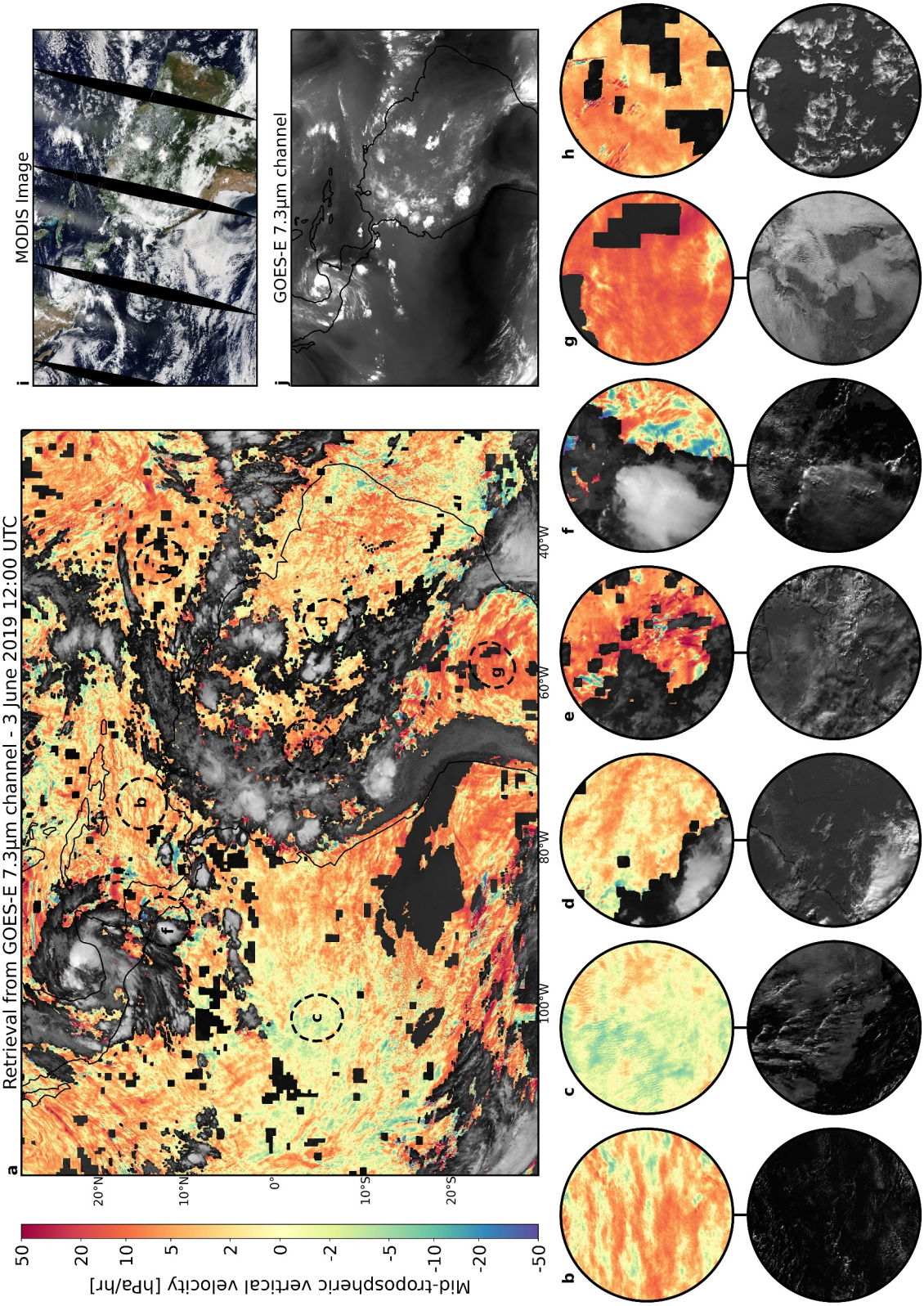

Figure 3. Vertical velocity retrieved on 3 June 2019 12:00UTC. Note the colorbar, linear between −2 and 2 $hPa \cdot hr^{-1}$ and logarithmic beyond. Brightness temperature in the infrared window channel (10.3 µm) is shown at places where the retrieval could not be performed, that is, mainly in regions of deep convection. (a) Retrieval from GOES-16. Panels (b)–(h) are zoomed versions of the circles labeled in (a). They have a diameter of 240px, which corresponds to about 600 km. They are accompanied with corresponding visible images at 800 nm. In panel c, the visible image is taken after sunrise at 14:00 UTC. (i) MODIS Terra True color image, taken at 10:30a.m.LST. (j) GOES-E brightness temperature in the 7.3 µm water vapor channel, from which vertical motion is deduced. (k)–(n) Full disk retrievals from various geostationary satellites.

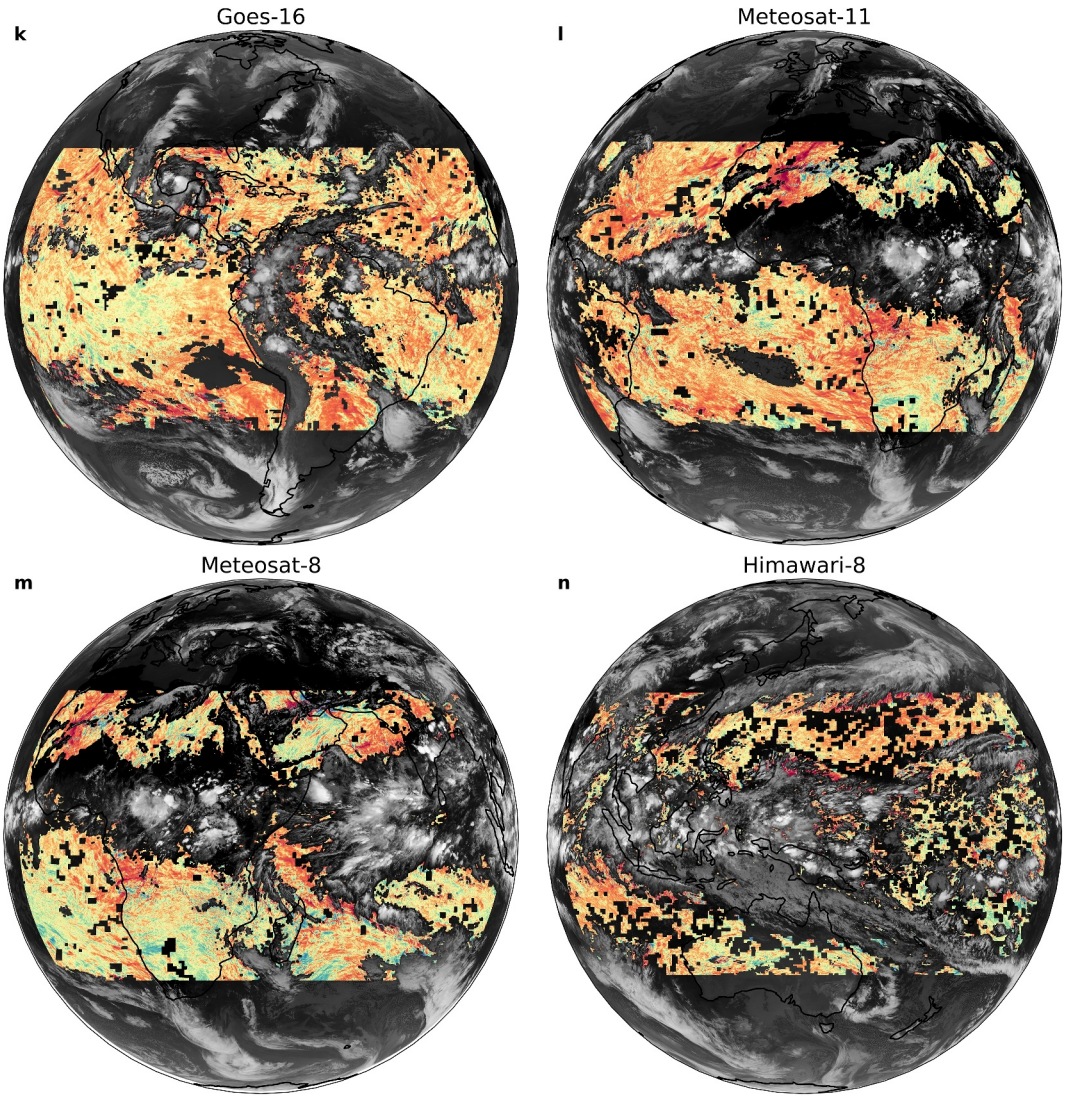

Figure 3. (Continued)

ascending/descending dipole along the equator between 120°W and 80°W is a Kelvin wave (not shown). Wave patterns (possibly gravity waves) are also visible on panels b and c with wavelengths of about 100 km and a few kilometers, respectively.

Another striking feature is the diversity of vertical velocity intensities in the vicinity of deep convection. Regions where convection is aggregated, such as the SouthWest of the Gulf of Mexico, the Northern Andes, or the Eastern Indian Ocean, are surrounded by relatively uniform and very strong subsidence (see zoom on panel e). This subsidence occurs within a few hundred kilometers from the convective systems, and is associated with vertical displacements that are about 20 times larger than those that would be expected from a radiative cooling of 1 $K \cdot day^{-1}$ (about 1 $hPa \cdot hr^{-1}$). Conversely, in regions where convection is disorganized, this strong subsidence is not always present (e.g., panel d). Panel f gives an example of more complex vertical velocity structures surrounding a convective system, that could be gravity waves generated by the system itself.

By combining these new observations with the visible channel and MODIS imagery, it is possible to investigate links between mid-tropospheric vertical motions and shallow convection located underneath. Inned, although shallow convection is not expected to be directly influenced mid-tropospheric vertical motion directly, the low-

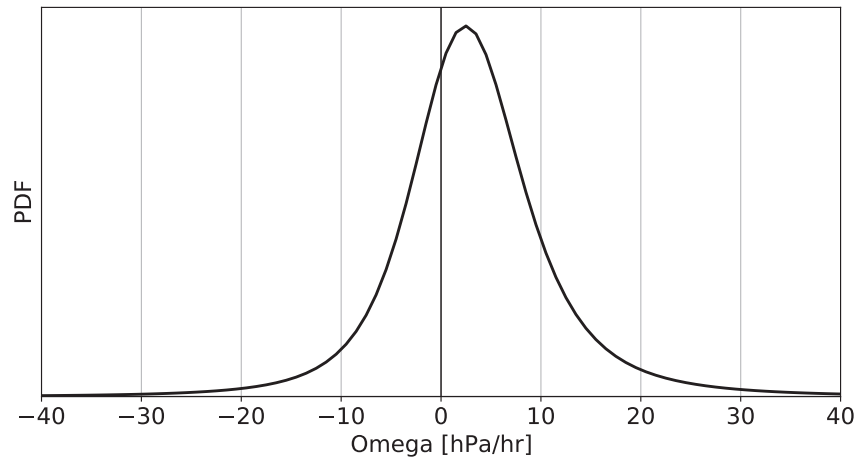

Figure 4. Distribution of vertical velocity values retrieved from Meteosat-11 during the year 2019.

level stability can respond to free tropospheric dynamics and, among a range of other factors, affect the development of shallow clouds. Let us first analyze these links over land. In the Amazon basin (panel d), subsidence is weak and shallow convective activity occurs with sporadic deep convection (panel i). Conversely, outside of circle d to the South East, in the Brazilian Highlands, mid-tropospheric subsidence is more pronounced and no shallow convection is present. Finally, over Gran Chaco (panel g), even stronger subsidence is found and it is associated with the presence of low stratocumulus clouds. Mid-tropospheric vertical motion may therefore play a role in controlling shallow convection over land, although these differences in low cloud cover are also likely controlled by differences in the surface turbulent fluxes. Ocean regions are associated with mesoscale cloud patterns that are reminiscent of those described by Stevens et al. (2020). Regions of ascendance or weak subsidence, such as panels b and c, are populated by sugar-like patterns (associated with a prominence of small, shallow cumuli). Conversely, more organized mesoscale patterns such as flowers are visible in panel h, associated with moderate subsidence (<10 hPa·hr^{-1}). Similarly, gravel patterns (open cells of precipitating cumuli) are associated with strong subsidence (10–30 hPa·hr^{-1}) in the South West of the domain, possibly associated with an extratropical intrusion. These observations are consistent with results from Schulz et al. (2021) (see their Fig. 14), and seem to support the role of the large-scale dynamics in playing a role in the control of shallow convection and its mesoscale organization.

Figure 4 shows the distribution of vertical velocity values retrieved from Meteosat-11 (located at 0°E). Consistently with Figure 3, the distribution peaks around 2h Pa·hr^{-1}, which corresponds to the subsidence expected from a radiative cooling rate of about 2 K/day. However, the spread of the distribution is significant and about a third of the values correspond to ascending motion, while 15% correspond to a subsidence exceeding 10 hPa·hr^{-1}.

5. Evaluation of the Retrieval

In the following, we evaluate our retrieval against observations to assess the physical credibility of the above features. The vertical motion retrievals are first evaluated using a perfect model approach to assess the methodology, and then against measurements from two field campaigns, both for convectively active and suppressed conditions.

5.1. Evaluation in a Perfect Model Approach

The retrieval method is first evaluated in a so-called perfect model approach using a week-long global simulation from the ICON coupled ocean-atmosphere model (Hohenegger et al., 2022; Klocke et al., 2017) without convective parameterization. We use instantaneous 3D output at 15-min resolution and at a native horizontal resolution of 9 km from a simulation performed as part of the NextGEMS project (https://nextgems-h2020.eu/).

Brightness temperatures in different geostationary satellite channels were computed using the radiative transfer code RTTOV version 13.2 (Saunders et al., 2018). Then, following a classical *model-to-satellite* approach (Morcrette, 1991), vertical motions were inferred from these simulated brightness temperatures using the same equations and approach as for the satellite observations (see Supporting Information S1 for technical details). This simulated retrieval is compared to the Lagrangian hourly average of vertical velocity at the emission level in the simulation.

As shown on Figures 5a and 5b, the retrieval method is able to capture the spatial patterns of vertical velocity at the planetary scale. Most ascending and descending structures are correctly retrieved (notably over North and South America, in Central and South Africa, over Australia and in the Eastern Pacific). Apart from some features for which the amplitude of vertical motions is overestimated (notably an ascending region over the Eastern Sahara), the magnitude of vertical motions is also well captured. To further evaluate the performance of the method at smaller spatial scales, maps of simulated vertical velocity and the associated simulated retrieval are shown on Figures 5c–5j in a mesoscale region affected by deep convection. Mesoscale vertical motion patterns, as well as their time variability, are well captured. The retrieval method is even able to capture the presence of gravity wave trains forming rings of either ascendance or subsidence in the close vicinity of deep convection (e.g., 54°W 12°N in panels c, g; or 50°W 2°S in panels d, h). The magnitude of vertical motion caused by these waves is also very well captured. Note, however, the presence on panels b,g,k of some narrow regions in the close vicinity of the cloud mask (within 10 km) where spurious, strong and noisy vertical motion are retrieved: these are likely due to the presence of semitransparent clouds that have not been detected by the algorithm. Those regions only concern a small fraction of the domain, and could be the focus of future improvements in the method.

We further investigate the ability of the retrieval method to capture temporal variations of vertical velocity in figure 5k-l. Panel k shows the temporal evolution of vertical velocity averaged over two mesoscale circles with a diameter of 2 and 8°. These circles are centered over Barbados, to ease comparison with the observational-based validation presented in the next section. Situations where clouds occupied more than half of the box are omitted. The retrieval is able to capture the evolution of vertical motion and its variability from the hourly to the daily time scale, as it is also shown on panel l.

The perfect model approach is also the opportunity to test the importance of different components of the retrieval. In particular, it is shown in Figure S2 in Supporting Information S1 that the effect of horizontal advection is strong enough that it cannot be neglected.

5.2. Evaluation Against Observations

The retrieval is now evaluated against observations. Its ability to capture spatial patterns of vertical motions is evaluated using observations from the OTREC campaign (Organization of Tropical East Pacific Convection; Fuchs-Stone et al. (2020)), and its ability to capture time variations is assessed using observations from the EUREC^{4}A campaign (ElUcidating the RolE of Cloud–Circulation Coupling in ClimAte; Bony et al. (2017); Stevens et al. (2021)). These two campaigns are associated with very different atmospheric conditions: EUREC^{4}A sampled regimes of shallow convection in a trade wind environment, while OTREC sampled deep convection and the ITCZ.

5.2.1. Spatial Variability During OTREC

The OTREC field campaign (Fuchs-Stone et al., 2020) took place over the Eastern Pacific and Caribbean sea during August-October 2019, in the vicinity of the ITCZ. During the campaign, dropsondes were released every 5–10 min in a grid pattern with a resolution of about 100 km (Vömel et al., 2021). This dropsonde data set was then used by Raymond and Fuchs-Stone (2021) to estimate vertical velocity fields from mass conservation, which is expected to have an effective resolution of 1°.

Figure 6 compares vertical velocity retrievals from GOES (using the methodology presented above) with estimates from dropsondes for 12 August and 22 August 2019, the only two days when an area of clear sky wide by several hundreds of kilometers was sampled during the campaign. The retrieval is able to reproduce the average value of vertical motion, and the three data sets agree within the 95% confidence interval of the retrieval over almost the whole domain.

10.1029/2024AV001267

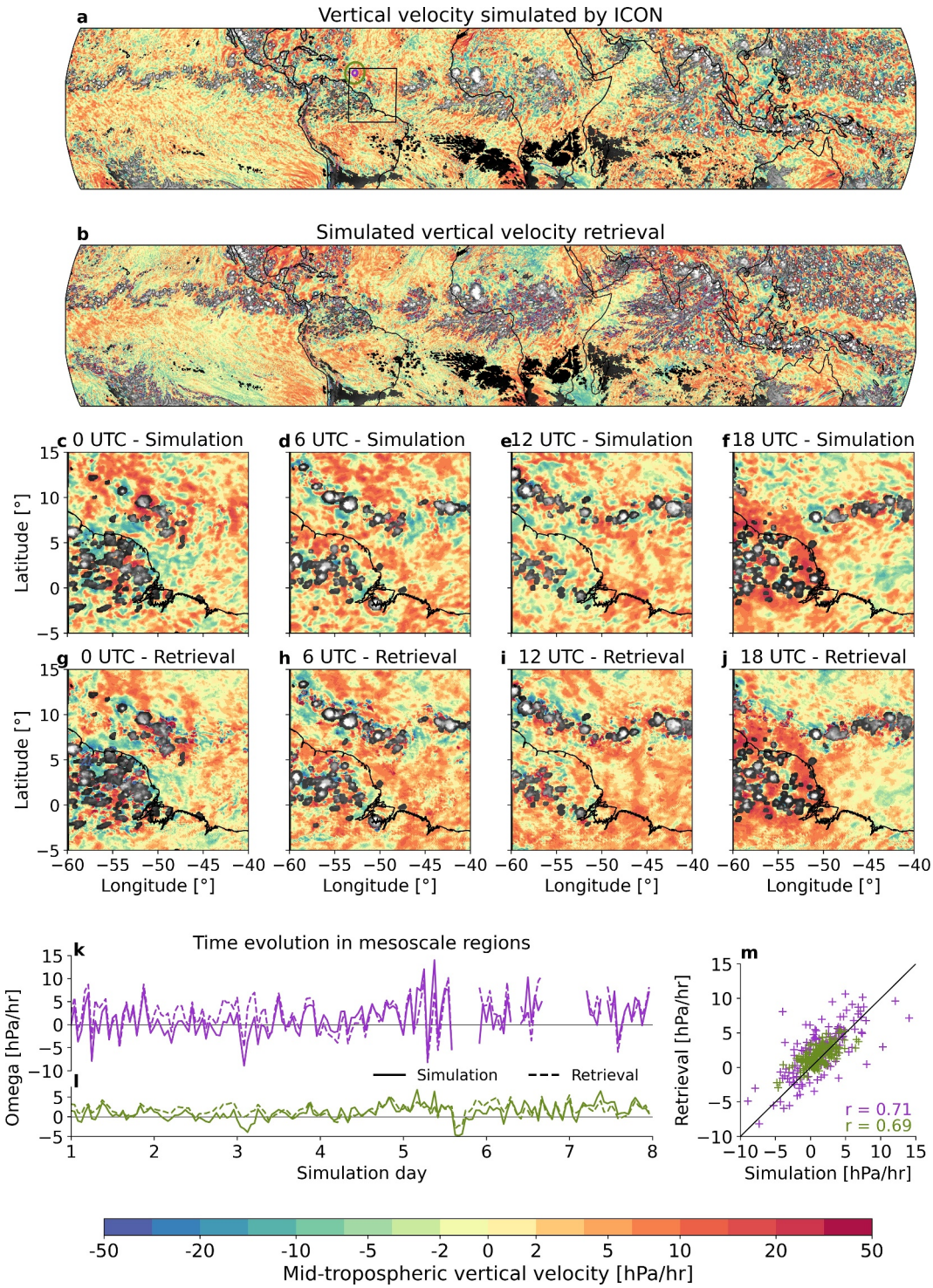

Figure 5. Evaluation in a perfect model approach. (a) Vertical motion in the simulation on 1 July 2021, 00:00UTC. (b) Retrieval from simulated brightness temperatures and horizontal winds. (c)–(f) Mid-tropospheric vertical velocity simulated by ICON for different timesteps as indicated in the titles, and zoomed over the black box shown in (a). Panels (g)–(j) as (c)–(f) but for the simulated retrieval. In (a)–(j), vertical velocity was masked out in cloudy regions where the retrieval could not be performed. Brightness temperature in the infrared window channel is instead shown in those areas. (k)–(l) Time series of mean vertical velocity within the purple and green circles shown in panel (a). Solid lines correspond to the vertical velocity simulated by ICON, while dashed lines correspond to the simulated retrieval. (m) Scatter plot of simulated vertical velocity (x-axis) versus simulated retrieval (y-axis) within the purple and green circles.

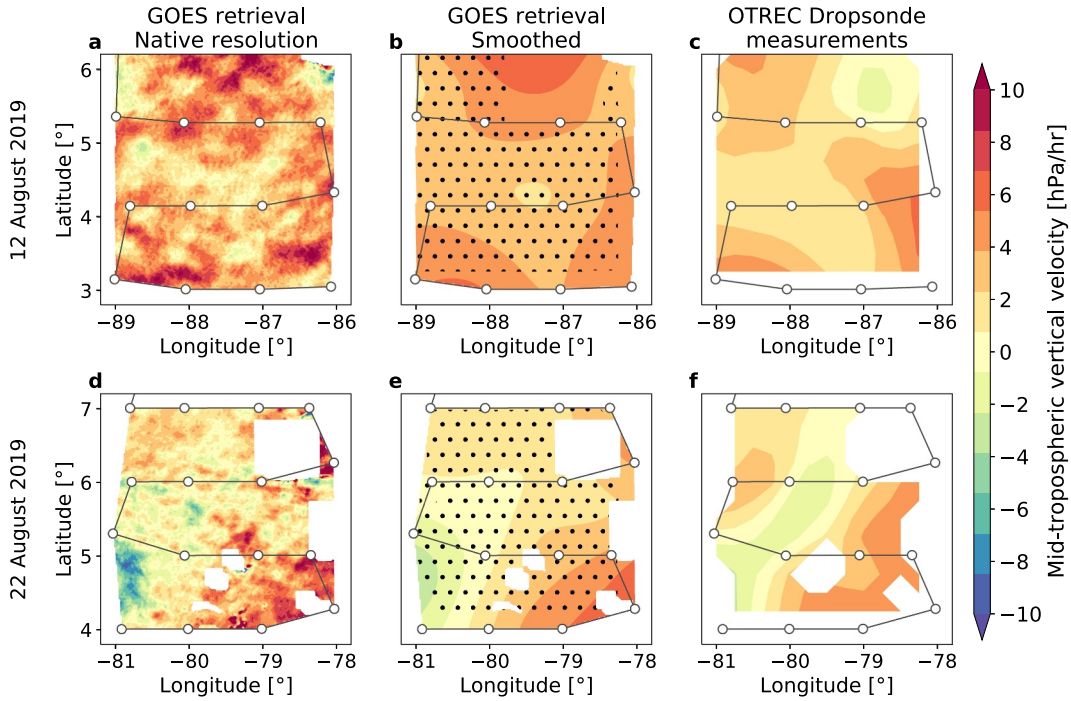

Figure 6. (a–c) Maps of mid-tropospheric vertical velocity during the OTREC flight of 12 August 2019. The flight track is represented in black, and white dots show the location of released dropsondes. (a) Vertical velocity retrieved from GOES. (b) Same, but smoothed at the resolution of dropsondes using a Gaussian kernel of half-width 50 km. (c) Vertical velocity from the dropsonde measurements obtained from mass conservation. Dots on panel (b) indicate that dropsonde measurements lie within the 95% confidence interval of the satellite observations. (d)–(f) Same as (a)–(c), but for the flight of 22 August 2019. All observations are shown at the emission level, which varies between 460 and 540 hPa.

Panel a shows the ubiquity of vertical motion structures that have a scale of a few dozens of kilometers, similar to the ones observed on Figure 3. When those structures are spatially averaged to the effective resolution of OTREC data (panel b), they become comparable to the patterns visible in the dropsonde data set, especially on August 22nd. On August 12th, the retrieval is able to capture the location of subsidence maxima in the Southern part of the domain, but agreement in the general pattern remains far from perfect, and the retrieval disagrees with the dropsondes in the Northeastern part.

The agreement, although satisfactory, is not as good as the one that was inferred from the perfect model approach. This may be due to observational noise and instrument limitations, that were not accounted for in the perfect model approach. However, in this case, part of the disagreement may also arise from the dropsonde measurements. Mesoscale regions of 1×1 degree are only circled by about 4 dropsondes, which can introduce a relatively large uncertainty in the vertical velocity estimate from mass conservation (Bony & Stevens, 2019). Moreover, this measurement is not well constrained in the mid-troposphere, because the error is cumulative with height. Therefore, it is unclear whether the disagreement between the two measurements in the Northern part of the domain on August 12th is due to errors in the satellite-based, in the dropsonde-based, or in both vertical motion retrievals.

5.2.2. Time Variability During EUREC^{4}A

The EUREC^{4}A field campaign (Bony et al., 2017; Stevens et al., 2021) took place during January-February 2020 East of Barbados, in the North Atlantic winter trades. It sampled typical subtropical conditions associated with various patterns of shallow convection (Stevens et al., 2020). During the campaign, the HALO aircraft flew repeated patterns along a circle of diameter 220 km (hereafter, the EUREC^{4}A circle) and released dropsondes intensively along its track (Konow et al., 2021). Using the method from Bony and Stevens (2019), George et al. (2021) derived area-averaged vertical velocity profiles from these dropsonde measurements. The repeated flight pattern of HALO is an opportunity to consider time variations of vertical motion over a fixed location.

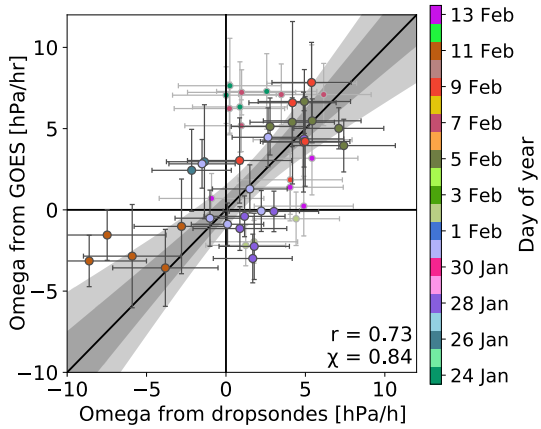

Figure 7. Evaluation of the satellite vertical velocity observations during the EUREC^{4}A field campaign. (a) Vertical velocity averaged by circling set as measured from dropsondes (x-axis) and satellite retrieval (y-axis), shown with their standard error. The dropsonde measurement is taken in a layer 200 hPa thick centered on the emission level (usually found between 400 and 600 hPa). Points with lighter error bars correspond to cold pool situations and are not included in statistical analysis. Confidence bands of an orthogonal distance linear regression are shown at one and two standard deviations. The $y = x$ line is shown in black. The Pearson's correlation coefficient as well as the reduced χ statistic are shown. The colorbar was designed with colorgorical (Gramazio et al., 2017).

Vertical velocity measurements were grouped by circling set, as vertical velocity was found to be consistent within these sets (George et al., 2023). Each circling set corresponds to two or three successive circles. 70 circles (24 circling sets and 12 flights) were flown over a period of about a month. This provides a sampling of daily and day-to-day variability over the campaign period.

In Figure 7, vertical velocity estimated from satellite is compared to vertical velocity measured from mass conservation by dropsondes, vertically averaged in a 200 hPa thick layer centered on the emission level (see Supporting Information S1 for technical details). For a significant fraction of the points, the error bars overlap the $y = x$ line which indicates that measurements from dropsondes and from satellite are statistically consistent, and the sign of the retrieved vertical velocity is correct for most of the points. Moreover, the $y = x$ line is embedded in the 95% confidence bands of the linear regression, demonstrating that the retrieval is able to capture the temporal variability of mesoscale vertical motions in a trade wind environment.

We note however a few days for which the agreement is less good (e.g. 2 February). These cases turn out to correspond to days during which many dropsondes fell in cold pools (identified with the methodology of Touzé-Peiffer et al. (2022); circling sets for which more than 10% of the soundings included a cold pool are shown with lighter error bars in the figure). We argue that in those cases, satellite measurements may be more reliable than dropsonde measurements from mass conservation. Indeed, local gust fronts are present at the edge of cold pools and can locally perturb the divergence estimates from the dropsonde motion. This error is then propagated upwards when divergence is vertically integrated. In the light of these considerations, cold pool situations were removed from the statistical analysis.

For a more quantitative evaluation of the agreement between observations, the χ statistic is reported on Figure 7, which measures the deviation from the $y = x$ line normalized by error bars (Andrae et al., 2010). Here, the reduced χ-value is close to 1, indicating that the retrieval is compatible with in situ observations modulo the error bars, and that these error bars are likely to be well estimated. The good agreement between the satellite measurements and the dropsonde data is an evidence for the quality of both data sets: if any of the two data sets was not able to capture mesoscale vertical motions, there would not be any correlation. The fact that the agreement is much better than for the OTREC data could be explained either by the more precise dropsonde vertical velocity data set (in this case 12 dropsondes were released along each circle), or by a better performance of the retrieval method in convectively suppressed conditions.

Note that dropsonde measurements from EUREC^{4}A were also used to evaluate intermediate steps of the retrieval, including:

- the retrieval of relative humidity at the emission level from brightness temperature ($0.65 \leq r \leq 0.89$ depending on channels, see Figure S1 in Supporting Information S1). This good performance shows that hypothesis (H2) is not a gross assumption.
- the retrieval of horizontal winds by cross-correlation (not shown). The method performs relatively well ($0.66 \leq r \leq 0.97$ depending on channels and wind component) and using wind measurements from dropsondes instead of satellite estimates did not improve significantly the results, showing that correction from advection is not the dominant source of error in the final product.

The evaluation is summarized with Taylor diagrams (Taylor, 2001) on Figure 8, where it is compared to the performance inferred from the perfect model approach. The diagrams have different references: dropsondes are the reference for the evaluation of the new satellite observations and ERA-5 (blue colors), whereas the ICON simulation is the reference for the retrieval of vertical velocity in the perfect model approach (red colors). See Text S5.5 in Supporting Information S1 for technical details on computation of correlation, root mean square vertical velocity, and their error bars.

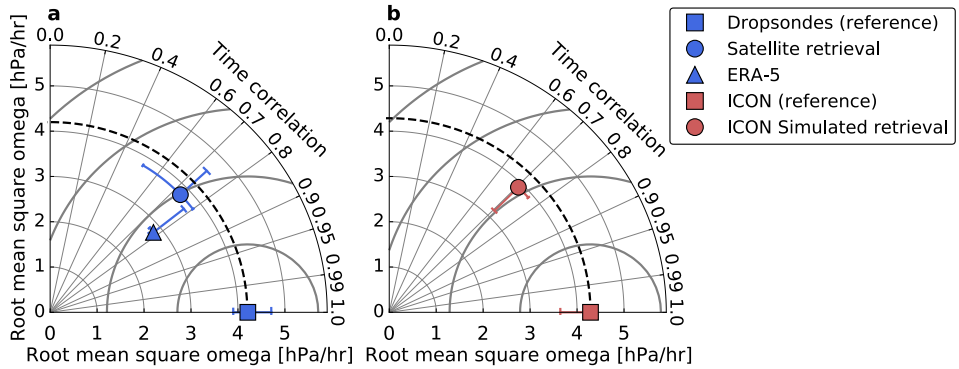

Figure 8. Taylor diagram presenting a synthetic analysis of vertical velocity estimates in the EUREC^{4}A region (purple circle on Figure 5a). The radius corresponds to root mean square of vertical velocity. The angle to the vertical corresponds to the correlation between each given data set, and the associated reference data set. (a) Observational evaluation against dropsonde measurements in convectively suppressed conditions. (b) Perfect model evaluation in convectively active conditions. See the supplement for the error bar computation. Dashed lines correspond to the amplitude of vertical motion in the reference data sets, and contours of root mean square error against reference data sets are also shown in gray. Code from Copin (2012) was used to produce this diagram.

The observed performance of the new observations against dropsondes (blue circle) corresponds well to the simulated performance at the mesoscale (red circle). Also, both in the perfect model approach and for in situ observations, the magnitude of vertical velocity variations inferred from satellite is realistic. This similarity between observed and simulated performances builds confidence into the retrieval methodology.

Overall, the performance of satellite retrievals is comparable to ERA-5. Note, however, that ERA-5 assimilated dropsonde data. Although some reanalysis experiments were conducted in which assimilation of dropsonde and radiosondes was denied (Savazzi et al., 2022), they could not be used here because the vertical velocity field was only stored at a 6-hourly timestep which is too coarse to be compared to values measured within the EUREC4A circle, that vary within a few hours. George et al. (2023) suggested that assimilation of radiosondes and dropsondes has overall a small impact on vertical velocity in the boundary layer in ERA-5, but it is not known whether this also applies to the free troposphere.

Unlike the satellite retrieval, ERA-5 underestimates the magnitude of vertical motion with respect to the dropsondes. Moreover, the satellite retrievals also have a much higher spatial resolution and a continuous sampling. These new, purely observational estimates of vertical velocity from space thus constitute an added value for characterizing vertical motions in the clear sky atmosphere.

6. Physical Processes Controlling Clear-Sky Vertical Motions

Given the good performance of the retrieval method, we now use the new observations to investigate the physical processes responsible for the rich diversity of vertical velocity patterns revealed in Figure 3. To that end, we first perform a spectral analysis to identify waves, and we then use radiosonde data to distinguish buoyancy-driven from radiatively driven vertical motions.

6.1. Spectral Analysis

6.1.1. Large-Scale Wave Activity

Takayabu (1994) and then Wheeler and Kiladis (1999) have shown that outgoing longwave radiation time-space spectra correspond well to the dispersion relationships of shallow-water equatorial waves, demonstrating the ubiquity of convectively coupled waves in the tropical atmosphere. Here, we take advantage of the high frequency and near-global coverage of the new vertical velocity observations to investigate the presence of such waves in the tropical clear sky by repeating their spectral analysis. See Supporting Information S1 (Text S5.1.1) for details on the spectrum computation. Note that we ensured, by reproducing the analysis on ERA-5 data with and without a cloud mask (not shown), that the spectral peaks obtained are not an artifact of the cloud mask.

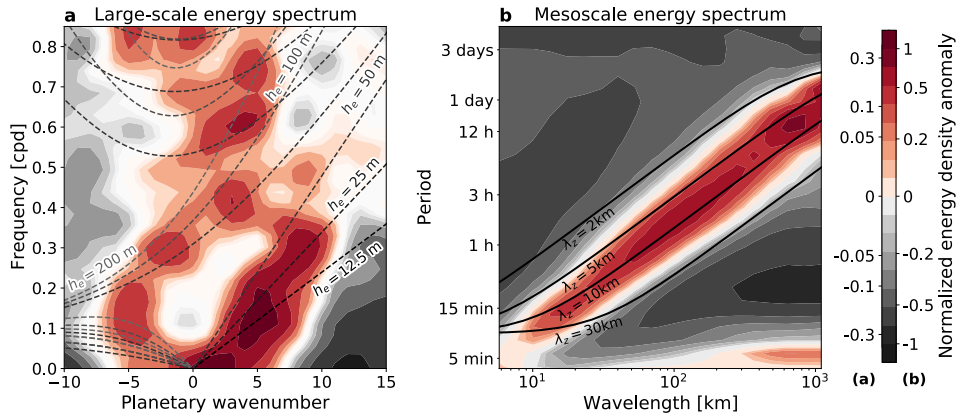

Figure 9. Energy spectra of mid-tropospheric vertical velocity retrievals at various spatial scales. A background spectrum S' was estimated by smoothing the energy spectrum S in the time axis, and shown is the normalized deviation to background spectrum $(S - S')/S'$. (a) Time-longitude energy spectrum of vertical velocity for the year 2019 in the whole tropical band (25°S–25°N). Overlaid are the dispersion relations of the first three modes of equatorial waves. Positive wavenumbers correspond to eastward propagation. Different line colors correspond to different equivalent depths h_e as indicated along the lines on the bottom right. Note that Kelvin waves were drawn for lower equivalent depths down to 12.5 m. (b) Time-space energy spectrum of vertical velocity during the EUREC^{4}A campaign, in the North Atlantic trade wind region. Overlaid is the dispersion relation of gravity waves. Different lines correspond to different vertical wavelengths, as indicated along the lines. Note the nonlinear colorbar on the right. Labels on both sides of the colorbar correspond to the two panels.

The obtained spectrum is shown on Figure 9a. Overlaid on it are the dispersion relationships of equatorial waves associated with various equivalent depths h_e of the atmosphere, defined as:

$$\frac{\sqrt{gh_e}}{\beta}\left(\frac{\Omega^2}{gh_e} - k_x^2 - \frac{\beta k_x}{\Omega}\right) = 2n + 1 \tag{16}$$

where n is the wave mode, k_x the zonal wave vector, β the beta-plane parameter, and Ω the wave pulsation (Matsuno, 1966). Vertical velocity retrievals reveal that Kelvin waves have a strong signal in the energy spectrum of mid-tropospheric clear-sky vertical motions at the planetary scale. Significant energy peaks are also present for westward propagating waves at low frequencies, that match well the dispersion curves of Rossby waves, as well as mixed Rossby-gravity waves. The Madden-Julian Oscillation (Madden & Julian, 1971) is visible at wavenumbers 1–4. Finally, some weaker activity is also visible at larger frequencies that could correspond to inertia-gravity waves. As indicated by Kiladis et al. (2009), values of h_e from 100 to 200 m for dry waves correspond to vertical wavelengths of 20–30 km, that correspond to about twice the depth of the troposphere (i.e., vertical mode 0). Here, the equivalent depths that match best the observed energy spectrum are about h_e = 12–50 m for Kelvin waves and h_e = 100–200 m for Rossby waves and mixed Rossby-gravity waves. This is slightly larger than the equivalent depth values observed for convectively coupled waves, as Wheeler and Kiladis (1999) observed a wave activity with $h_e \approx$ 12–25 m in Outgoing Longwave Radiation spectra, and suggests that equatorial waves could travel faster through clear-air regions than through convectively active regions as anticipated by Bony and Emanuel (2005). This is especially the case for Rossby and mixed Rossby-gravity waves.

6.1.2. Mesoscale Wave Activity

The retrieval does not only provide vertical motion estimates at the large scale, but also at the mesoscale. To investigate the origin of mesoscale motions, a similar analysis is conducted over a much smaller region. The selected area and period correspond to the EUREC^{4}A field campaign that took place during January-February 2020 East of Barbados, in the North Atlantic winter trades (approximately 48–63°W and 8–18°N). During the campaign, GOES-R brightness temperature images were available at a resolution of 1 min and 2 km in time and space, respectively. Vertical velocity was therefore estimated on a 1-min timestep. For this purpose, only two successive images were used to compute the time derivative of brightness temperature, instead of performing the linear regression as shown on Figure 2. Brightness temperature data was analyzed by separate 2-day blocks. For each of

these blocks, a spatio-temporal spectrum was computed on the native satellite grid. Then, the effect of large-scale horizontal advection on the spectrum was removed by translating the spectrum following the operation:

$$\Omega \leftarrow \Omega - \vec{u} \cdot \vec{k} \tag{17}$$

where Ω is the wave pulsation, $\vec{k}$ the horizontal wavenumber, and $\vec{u}$ the average horizontal wind measured by radiosondes and dropsondes during that 2-day period in the mid-troposphere (4–6 km). Finally, the energy spectra from all the blocks were added to provide a final energy spectrum corrected from advection. The fully non-hydrostatic dispersion relationship of gravity waves is drawn on the spectrum:

$$\left(\Omega - \vec{u} \cdot \vec{k}\right)^2 = f^2 \frac{m^2 + \frac{1}{4H^2}}{m^2 + \vec{k}^2 + \frac{1}{4H^2}} + N^2 \frac{\vec{k}^2}{m^2 + \vec{k}^2 + \frac{1}{4H^2}} \tag{18}$$

where f is the Coriolis parameter, and H is the characteristic density decay vertical scale of the atmosphere. N^2 is the time-averaged Brunt-Väisälä frequency measured during the campaign in the mid-troposphere. The lines were drawn for different vertical wavenumbers m, corresponding to different vertical wavelengths λ_z.

The power spectrum, shown on Figure 9b, follows the dispersion relationship of gravity waves that would have a vertical wavelength of 2–30 km, that is, coherent structures of vertical velocity that have a thickness ranging from 1 km (the approximate depth of the water vapor channel weighting function) up to 15 km (the depth of the troposphere). Note that, as most methods based on passive radiance measurements, our retrieval is unable to capture features with a fine vertical structure due to hypothesis (H8). Gravity waves of shorter vertical wavelengths may be present, but they cannot be detected. In particular, the two cutoff frequencies predicted by the theory (Eckart, 1960), namely the Brunt-Väisälä frequency and the inertial frequency, are also cutoff frequencies for the observed vertical motions. This spectrum indicates that gravity waves dominate the tropical energy spectrum of clear-sky air velocity at time scales from minutes to days. This comforts previous results that have shown that tropical mesoscale vertical motion was consistent with gravity waves (Bony & Stevens, 2019; Stephan et al., 2020). It also demonstrates the ability of the new satellite observations to capture gravity waves at spatial scales spanning several orders of magnitude. The spectrum exhibits three local maxima of energy in gravity waves, suggesting a possible resonance of gravity waves with scale selection processes at different spatial and temporal frequencies:

- the Brunt-Väisälä frequency (about 10 min)
- the diurnal cycle
- the mesoscale (30 min-6 hr; 30–300 km). The cause of this energy maximum remains to be investigated.

Overall, this spectral analysis demonstrates the importance of gravity waves in controlling vertical motions in the tropical clear sky, and provides a possible explanation for the large variance of vertical velocities observed at the mesoscale.

6.2. Buoyancy-Driven and Radiatively Driven Vertical Motion

Gradients in radiative cooling are believed to also play a role in tropical mesoscale shallow circulations (Naumann et al., 2017, 2019; Schulz & Stevens, 2018; Yang, 2021). To disentangle the role of gravity waves from the role of radiative cooling, vertical profiles of virtual temperature and clear-sky radiative cooling computed from dropsondes and radiosondes launched during the EUREC^{4}A campaign (Albright et al., 2021; George et al., 2021; Stephan et al., 2021) were analyzed along with the new observations of mid-tropospheric vertical velocity.

To evaluate buoyancy at the mesoscale, it is possible to take advantage of the circular flight pattern of HALO during the campaign as shown on Figure 10c. For each flight circle, 12 dropsondes were released. For each dropsonde, a virtual temperature anomaly with respect to the circle mean profile is computed. The anomaly is then averaged vertically in a 2 km thick layer centered on the emission level. It is compared to a vertical velocity anomaly, estimated from the new satellite observations by computing the average vertical velocity within 110 km around the dropsonde of interest (orange area on panel c) and substracting the average vertical velocity around the circle (gray area on panel c). To ensure a maximal correlation between buoyancy and vertical motion, the vertical

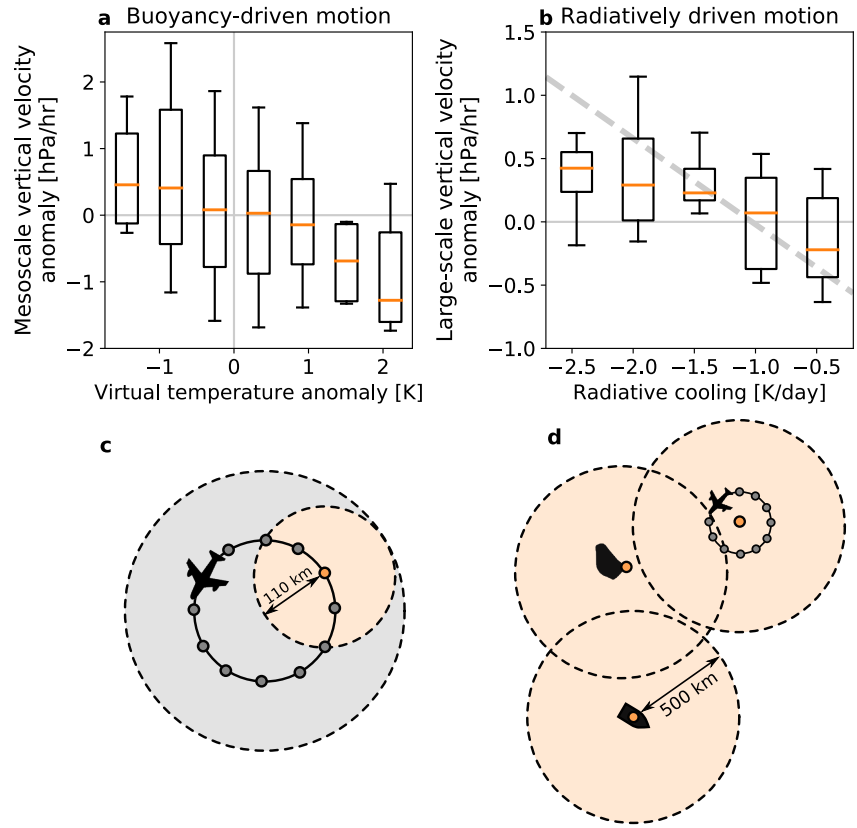

Figure 10. Relationship between vertical velocity, buoyancy, and radiative cooling during the EUREC^{4}A field campaign. (a) Mesoscale vertical velocity anomaly binned by virtual temperature anomaly for each HALO circle. (b) Large-scale vertical velocity anomaly binned by radiative cooling rate from dropsondes and radiosondes. The light gray slope corresponds to the theoretical prediction. (c–d) Schematics showing how vertical velocity is computed for panels a and b, respectively. See the main text for details. In Panels (a)–(b), the number of bins was chosen to ensure that at least 10 samples are present for each bin.

velocity is taken with a phase shift of $\pi/2$ with respect to virtual temperature. This is achieved by taking vertical velocity with a delay corresponding to the quarter of the period of a gravity wave of vertical mode 1, the half-wavelength of which corresponds to the diameter of the orange circle in panel c. This phase shift is expected because temperature is related to the time derivative of vertical velocity.

As shown in Figure 10a, upward anomalies are associated with warmer virtual temperatures in the mid-troposphere, and conversely. Buoyancy variations appear to explain a significant part of the variability of mesoscale vertical velocity anomalies, which suggests that at the mesoscale, free tropospheric vertical motions are mostly buoyancy-driven and that the observed correlation may indeed be due to the presence of gravity waves. Conversely, we do not observe significant correlation between mesoscale vertical velocity anomalies and the radiative cooling rate (not shown).

Similarly, to evaluate the link between vertical velocity and the measured vertical profiles on the large scale, the different platforms can be used. For each sounding (either radiosondes launched from the Barbados Cloud Observatory, from a ship, or dropsondes launched from HALO), the radiative cooling rate is averaged in a 2 km thick layer centered on the emission level. This radiative cooling rate is compared to the large-scale vertical velocity anomaly, that is, vertical velocity averaged in a circle of radius 500 km centered on the profile (see Figure 10d) to which mean vertical velocity over the retrieval domain is subtracted. Because individual dropsondes launched by HALO are not assumed to be independent from each other, the mean vertical profile of each HALO circle is used as a single sounding.

As shown on Figure 10b, downward anomalies correspond to larger radiative cooling above the emission level (i.e., in the upper troposphere). This suggests that at a scale of 500 km, vertical motion could be partly radiatively driven. Using a back-of-the-envelope computation, radiatively driven vertical velocity is easily estimated as:

$$\omega = \frac{pg\theta}{R_d T^2} \frac{Q_{rad}}{\mathrm{d}\theta/\mathrm{d}z} \tag{19}$$

The slope predicted by this relationship, shown in dashed gray, has the same order of magnitude than the observed slope. This places radiative cooling as a good candidate for the cause of vertical motions at the large scale. However, the relationship shown in Figure 10b is not very robust due to the small number of samples (about 10 samples per bin), so this conclusion must be taken with caution. Moreover, other mechanisms (including equatorial waves) probably also play an important role in controlling large-scale vertical velocity.

Overall, this analysis shows that gravity waves are a dominant source of vertical motion at the mesoscale (Figures 9b and 10a), while radiative cooling (Figure 10b) and equatorial waves (Figure 9a) may play a significant role in controlling large-scale vertical motion. This justifies the scale separation between vertical motions of different nature that is done in the last step of the implementation of the vertical velocity retrieval (Section 3.3). It also indicates that gravity waves may play an important role in the mid-tropospheric dynamics of shallow convective regimes, that typically occurs at the meso-β scale (20–200 km), whereas radiatively driven circulations may also play a significant role in the organization of deep convection in the ITCZ that occurs at slightly larger scales (typically the meso-α scale, 200–2,000 km).

7. Conclusion and Discussion

This study shows that it is now possible to measure vertical velocity from space using high rate geostationary satellite radiance measurements in the water vapor absorption band. We have shown that brightness temperature temporal variations can be quantitatively related to vertical velocity at the emission level. Apart from few situations with a very dry mid-troposphere, the satellite retrievals are at least as reliable as ERA-5 in terms of spatial and temporal variability. This makes it possible to retrieve vertical velocity continuously, over large domains and at high spatial and temporal resolution, thus filling a long-standing gap in atmospheric observations.

7.1. Toward a Better Understanding of Cloud-Circulation Coupling

These new satellite observations bring their share of surprises. First, they show that vertical motions in the clear-sky atmosphere are far from the *gentle subsidence* discussed in a range of studies and textbooks (e.g., Emanuel et al., 1994). On the contrary, we show that they can be strong and highly variable, exhibiting a rich diversity of patterns from the kilometer-scale to the planetary scale. George et al. (2023) have already pointed out the ubiquity of mesoscale vertical motions in the lower troposphere. Here, we show that in the mid-troposphere, vertical velocities can have a strong magnitude, with 15% of values exceeding 10 hPa·hr^{-1}, thereby supporting and generalizing the results of Bony and Stevens (2019). Although the clear air is mostly subsiding, transient ascents up to 200 hPa·day^{-1} can be measured over clear-sky regions of dozens to hundreds of kilometers (35% of the values are negative, and 5% are below -10 hPa·hr^{-1}).

We also show that around aggregated clusters of deep convection, strong subsidence (>20 hPa·hr^{-1}) is observed within a radius of a few hundred kilometers. This subsidence is more than an order of magnitude larger than subsidence that would be expected from a typical radiative cooling of 2 K/day. This suggests that subsidence around deep convection may be buoyancy-driven as proposed by Mapes (1993), or that radiative cooling rates are much stronger than previously believed in the vicinity of deep convection. This subsidence is found to persist for several hours, and can therefore produce substantial vertical displacements that could affect significantly atmospheric stability and humidity.

Overall, these new observations reveal that at the mesoscale, the variability of free tropospheric vertical motions is dominated by gravity waves. Conversely, at scales of 500 km or more, dynamics appear more complex and radiative cooling and equatorial waves may both play a significant role in controlling vertical motion. Note that it does not preclude that radiative cooling may play a more important role in the control of shallow circulations, notably at the boundary layer top where radiative cooling values can be much larger (Fildier et al., 2023; Naumann et al., 2017).

Although gravity waves are believed to play a role in the organization of deep and shallow convection (Lane & Clark, 2002; Mapes, 1993; Muller et al., 2022), most of convective aggregation research currently focuses on radiative feedbacks. Our results call for further research on the role of equatorial and gravity waves in shaping convective organization at the mesoscale and even at the large scale. Gravity wave activity and its interaction with convection have already been studied in detail in numerical simulations (Peatman et al., 2023) or in conceptual models (Yang, 2021). The satellite retrievals of vertical velocity presented here open the possibility to complement our knowledge with observational investigations.

7.2. A Range of Possible Uses in the Modeling Community

Beside fundamental studies on the organization of convection, the new vertical velocity measurements could serve other scientific issues and communities. For instance, mesoscale information is crucial for weather forecasting in the tropics, where predictability time scales are believed to be long (Stevens et al., 2019; Straus & Paolino, 2008), but forecasts are hampered by the lack of dynamical observations such as winds (Bechtold, 2019). The new observations could potentially be valuable for data assimilation in numerical weather prediction models, since they provide an estimate of vertical velocity over about 40% of the tropics at any given time, and error bars were found to be well estimated (Figure 7).

Owing to their high resolution in space and time, these observations are also an excellent opportunity to evaluate the performance of the new generation of global kilometer-scale climate models (Stevens et al., 2019). A new type of more complex, physically based evaluation of these models now becomes possible, with the possibility to compare gravity wave activity or cloud-circulation coupling between simulations and observations.

7.3. Perspectives for the Next Satellite Generations

The new vertical velocity observations provide information in the clear sky, that complements existing observations of the cloudy sky (e.g., composites of mass flux within convective clouds; Masunaga and Luo (2016); Jeyaratnam et al. (2021)). Several projects of space missions are under development that aim to measure in-cloud mass flux and vertical velocity (Brogniez et al., 2022; van den Heever et al., 2022). Knowing both clear-sky and in-cloud vertical velocity will enable to build a complete picture of the horizontal structure of mesoscale circulations and their coupling to deep convection. Moreover, the analytical relationships developed in this work could possibly be used to retrieve vertical velocity estimates both in and outside clouds, using variations of brightness temperature in the microwave spectral domain.

Note also that the retrieval method works on broad geostationary satellite channels because the final equation is independent on the spectroscopic coefficient κ. The fundamental cause of this behavior is that the Clausius-Clapeyron relation is exponential, which is the case for water but also for any other condensable gas, due to basic thermodynamics. (Indeed, relative humidity depends on κ in Equation 2 but a cancellation of κ in the computation occurs later in the derivation because temporal variations of relative humidity are exponential (Equation 4) and therefore vertical velocity is proportional to logarithmic variations in relative humidity.) As a result, similar retrievals could theoretically be performed on other planetary atmospheres experiencing moist convection, provided that this moist convection fixes the lapse rate of the atmosphere, and brightness temperature is measured in the absorption band of the condensable gas of interest. It could be an interesting perspective for potential projects of aerostationary satellites around solar system planets (Montabone et al., 2020).

Finally, the advent of a new generation of geostationary satellites will be an opportunity to further exploit the new vertical velocity retrieval presented here. High-rate hyperspectral measurements will provide a larger number of channels within the water vapor absorption band, thereby making it possible to retrieve vertical velocity profiles with a vertical resolution of about 2 km (the approximate thickness of the emission layer). Since an analytical relationship is available that relates changes in brightness temperature to vertical velocity, it may even be possible to use forward modeling and Bayesian inversion techniques to retrieve profiles at a higher vertical resolution. Although the actual feasibility of such vertical velocity profile retrievals from high-rate geostationary hyperspectral measurements remains to be evaluated, especially in terms of required computational resources, this retrieval could complement the vertical profiles of horizontal winds that will be available from hyperspectral geostationary sounders (Borde et al., 2019). The perspective of providing a spaceborne estimate of the three components of wind at high temporal, horizontal, and vertical resolution in the tropical atmosphere has never been so close.

Appendix A: Mathematical Notations

See Table A1.

Table A1
Mathematical Notations

τ	Optical thickness (vertical coordinate)	No unit
τ_S	Optical thickness of the atmosphere	No unit
κ	Extinction coefficient of water vapor	$m^2 \cdot kg^{-1}$
λ	Radiation wavelength	m
p	Pressure	hPa
q	Specific humidity	$kg \cdot kg^{-1}$
q_{sat}	Saturated specific humidity	$kg \cdot kg^{-1}$
e_{sat}	Water vapor saturation pressure	hPa
$w(p)$	Column water vapor above pressure p	$kg \cdot m^{-2}$
R_d	Specific perfect gas constant for dry air	$J \cdot K^{-1} \cdot kg^{-1}$
R_v	Specific perfect gas constant for water vapor	$J \cdot K^{-1} \cdot kg^{-1}$
L_v	Latent heat of vaporization of water	$J \cdot kg^{-1}$
Γ_m	Moist adiabatic lapse rate	$K \cdot m^{-1}$
Γ_d	Dry adiabatic lapse rate	$K \cdot m^{-1}$
Γ	Euler Gamma function	No unit
ϵ	Ratio between molar mass of water and dry air	No unit
ℓ	Laplace coefficient of dry air	No unit
k	$1 - 1/\ell$	No unit
RH	Relative humidity	No unit
T	Temperature	K
T_v	Virtual temperature	K
T^*	Air temperature at emission level	K
θ^*	Dimensionless temperature at emission level	No unit
θ	Potential temperature	K
Q_{rad}	Radiative cooling rate	K/day
T_s	Brightness temperature in the atmospheric window	K
B_λ	Planck function	$W \cdot m^{-2} \cdot sr^{-1} \cdot m^{-1}$
B_{sat}	Radiance measured from space in the water vapor channel	$W \cdot m^{-2} \cdot sr^{-1} \cdot m^{-1}$
ζ	Solar zenith angle	rad
μ	1/cos(Satellite zenith angle)	No unit
h	Planck constant	J·s
c	Speed of light	$m \cdot s^{-1}$
k_B	Boltzmann constant	$J \cdot K^{-1}$
t	Time	s
t_ω	Characteristic drying or moistening time	s
ω	Vertical pressure velocity	$hPa \cdot hr^{-1}$
$\vec{u}$	Horizontal velocity	$m \cdot s^{-1}$
Ω	Wave pulsation	s^{-1}
$\vec{k}$	Horizontal wave vector	m^{-1}
k_x	Zonal wave vector	m^{-1}
m	Vertical wave vector	m^{-1}

Table A1
Continued

n	Wave order	No unit
λ_z	Vertical wavelength	m
h_e	Equivalent depth	m
g	Gravitational acceleration	$m{\cdot}s^{-2}$
N	Brunt-Väisälä frequency	s^{-1}
f	Coriolis parameter	s^{-1}
β	β-plane parameter	$s^{-1}{\cdot}m^{-1}$
α	Defined as $B_\lambda(T) \propto T^\alpha$	No unit
β	Defined as $\tau \propto p^\beta$	No unit
γ	Defined as $B_\lambda(T) \propto \tau^\gamma$	No unit
δ	Defined as $p \propto T^\delta$	No unit
r	Pearson's correlation coefficient	No unit
χ	Normalized root mean square error	No unit
$\mathcal{N}$	Number of independent measurements	No unit
$\mathcal{G}(\sigma)$	Gaussian kernel of standard deviation σ	No unit

Environmentally Responsible Research

Dropsonde measurements from a research aircraft are increasingly used to measure vertical velocity profiles at the mesoscale (e.g., Bony and Stevens (2019); Raymond and Fuchs-Stone (2021); George et al. (2021)). This study shows that in the mid-troposphere, the accuracy of vertical velocity retrievals from space is comparable to that of dropsonde measurements. Moreover, unlike most space missions, geostationary satellite data is considered as having a negligible contribution to the carbon footprint of academic research (Marc et al., 2024). With the advent of geostationary satellite sounders, it might become possible, using the method proposed in this article, to infer vertical profiles of vertical velocity over a range of spatial and temporal resolutions. Therefore, measuring vertical velocities from space may become an interesting low-carbon alternative to dropsonde observations, and help reduce the environmental impact of academic research.

Conflict of Interest

The authors declare no conflicts of interest relevant to this study.

Data Availability Statement

GOES geostationary satellite images from the Advanced Baseline Imager (Schmit et al., 2017) used to apply the technique are available from NOAA at the following link: https://www.ncdc.noaa.gov/airs-web/search. Meteosat satellite images are available from the EUMETSAT data centre at https://data.eumetsat.int/product/EO:EUM:DAT:MSG:HRSEVIRI and https://data.eumetsat.int/product/EO:EUM:DAT:MSG:HRSEVIRI-IODC for the 0° and IODC missions, respectively. Himawari satellite images (Bessho et al., 2016) are available from the Japan Meteorological Agency (https://www.jma.go.jp/jma/jma-eng/satellite/dissemination.html). Vertical velocity data retrieved from dropsondes during the OTREC campaign is available at the following https://doi.org/10.5281/zenodo.5152171. GOES-R images at high temporal and spatial resolution, as well as the JOANNE data set (George et al., 2021) and the radiosonde data sets (Albright et al., 2021; Stephan et al., 2021) are available from the AERIS EUREC^{4}A data archive at https://eurec4a.aeris-data.fr/. The NARVAL simulation data is stored at the German Climate Computing Center (DKRZ) and can be made available upon request. The RTTOV software (Saunders et al., 2018) used to simulate satellite radiances can be found at https://nwp-saf.eumetsat.int/site/software/rttov/rttov-v13/. MODIS satellite images (Salomonson et al., 1989) can be downloaded from https://worldview.earthdata.nasa.gov/. The code used to produce the vertical velocity observations from brightness temperature netCDF files is available at https://doi.org/10.5281/zenodo.12686667 (Poujol & Bony, 2024). It requires geolocated brightness temperature files as an input, and provides estimations of vertical velocity, its standard error, as well as

the temperature and pressure at the emission level. Finally, ongoing work focuses on producing an archive of clear-air vertical velocity data based on Meteosat Second Generation radiances, that will be available from 2002 onwards.

Acknowledgments

We would like to thank Jean-Louis Dufresne, Rémy Roca, Raphaela Vogel, Geet George, Caroline Muller and Hirohiko Masunaga for insightful discussions and for their useful suggestions. Notably, JLD suggested to introduce pressure broadening in the computation, and RR suggested to implement a detection of semi-transparent clouds. We also thank Daniel Klocke and the ICON team for running the ICON simulation and making it available, and David Raymond for providing us dropsonde data from the OTREC field campaign. We gratefully acknowledge Brian Soden and an anonymous reviewer for their useful comments, which helped to significantly improve the study. We acknowledge the École Normale Supérieure (ENS-PSL, Paris, France) for the PhD fellowship of BP, as well as funding from the European Research Council (ERC Advanced Grant MAESTRO, grant agreement no 101098063) and the European Union's Horizon 2020 research and innovation program (nextGEMS project, grant agreement no 101003470). This study benefited from the IPSL Data and Computing Center ESPRI which is supported by CNRS, Sorbonne Université, CNES and École Polytechnique. This work used resources of the Deutsches Klimarechenzentrum (DKRZ) granted by its Scientific Steering Committee (WLA) under project ID bb1153. The authors gratefully acknowledge the ESPRI and DKRZ teams for their support in accessing the data and the resources. We also thank the French national center for Atmospheric data and services AERIS for maintaining data sets from the EUREC^{4}A field campaign.

References

Adames, Á. F. (2022). The basic equations under weak temperature gradient balance: Formulation, scaling, and types of convectively coupled motions. *Journal of the Atmospheric Sciences*, *79*(8), 2087–2108. https://doi.org/10.1175/jas-d-21-0215.1

Adames, Á. F., Powell, S. W., Ahmed, F., Mayta, V. C., & Neelin, J. D. (2021). Tropical precipitation evolution in a buoyancy-budget framework. *Journal of the Atmospheric Sciences*, *78*(2), 509–528. https://doi.org/10.1175/jas-d-20-0074.1

Albrecht, F. (1930). Der Wärmeumsatz durch die Wärmestrahlung des Wasserdampfes in der Atmosphäre. *Z. f. Geophys*, *421*.

Albright, A. L., Fildier, B., Touzé-Peiffer, L., Pincus, R., Vial, J., & Muller, C. (2021). Atmospheric radiative profiles during EUREC^{4}A [Dataset]. *Earth System Science Data*. https://essd.copernicus.org/articles/13/617/2021/

Andrae, R., Schulze-Hartung, T., & Melchior, P. (2010). Dos and don'ts of reduced chi-squared. *arXiv preprint arXiv:1012.3754*.

Augstein, E., Riehl, H., Ostapoff, F., & Wagner, V. (1973). Mass and energy transports in an undisturbed Atlantic trade-wind flow. *Monthly Weather Review*, *101*(2), 101–111. https://doi.org/10.1175/1520-0493(1973)101<0101:maetia>2.3.co;2

Bannon, J. (1949). Large-scale vertical motion in the atmosphere. *Nature*, *163*(41–43), 495–496.

Bechtold, P. (2019). Challenges in tropical numerical weather prediction at ECMWF. In *Current trends in the representation of physical processes in weather and climate models* (pp. 29–50).

Bellon, G., & Coppin, D. (2022). Sensitivity of convective self-aggregation to subsidence. *Journal of Advances in Modeling Earth Systems*, *14*(12), e2021MS002830. https://doi.org/10.1029/2021ms002830

Bessho, K., Date, K., Hayashi, M., Ikeda, A., Imai, T., Inoue, H., et al. (2016). An introduction to Himawari-8/9—Japan's new-generation geostationary meteorological satellites [Dataset]. *Journal of the Meteorological Society of Japan. Ser. II*, *94*(2), 151–183. https://doi.org/10.2151/jmsj.2016-009

Bjerknes, V. (1904). Das Problem der Wettervorhersage, betrachtet vom Standpunkte der Mechanik und der Physik. *Meteorologische Zeitschrift*, *21*, 1–7.

Bony, S., & Dufresne, J.-L. (2005). Marine boundary layer clouds at the heart of tropical cloud feedback uncertainties in climate models. *Geophysical Research Letters*, *32*(20), L20806. https://doi.org/10.1029/2005gl023851

Bony, S., & Emanuel, K. A. (2005). On the role of moist processes in tropical intraseasonal variability: Cloud–radiation and moisture–convection feedbacks. *Journal of the Atmospheric Sciences*, *62*(8), 2770–2789. https://doi.org/10.1175/jas3506.1

Bony, S., Lau, K., & Sud, Y. (1997). Sea surface temperature and large-scale circulation influences on tropical greenhouse effect and cloud radiative forcing. *Journal of Climate*, *10*(8), 2055–2077. https://doi.org/10.1175/1520-0442(1997)010<2055:sstals>2.0.co;2

Bony, S., & Stevens, B. (2019). Measuring area-averaged vertical motions with dropsondes. *Journal of the Atmospheric Sciences*, *76*(3), 767–783. https://doi.org/10.1175/jas-d-18-0141.1

Bony, S., Stevens, B., Ament, F., Bigorre, S., Chazette, P., Crewell, S., et al. (2017). EUREC^{4}A: A field campaign to elucidate the couplings between clouds, convection and circulation. *Surveys in Geophysics*, *38*(6), 1529–1568. https://doi.org/10.1007/s10712-017-9428-0

Bony, S., Stevens, B., Frierson, D. M., Jakob, C., Kageyama, M., Pincus, R., et al. (2015). Clouds, circulation and climate sensitivity. *Nature Geoscience*, *8*(4), 261–268. https://doi.org/10.1038/ngeo2398

Borde, R., Carranza, M., Hautecoeur, O., & Barbieux, K. (2019). Winds of change for future operational AMV at EUMETSAT. *Remote Sensing*, *11*(18), 2111. https://doi.org/10.3390/rs11182111

Bretherton, C. S., Blossey, P. N., & Khairoutdinov, M. (2005). An energy-balance analysis of deep convective self-aggregation above uniform SST. *Journal of the Atmospheric Sciences*, *62*(12), 4273–4292. https://doi.org/10.1175/jas3614.1

Brogniez, H., Roca, R., Auguste, F., Chaboureau, J.-P., Haddad, Z., Munchak, S. J., et al. (2022). Time-delayed tandem microwave observations of tropical deep convection: Overview of the C2OMODO mission. *Frontiers in Remote Sensing*, *3*, 854735. https://doi.org/10.3389/frsen.2022.854735

Charney, J. G. (1963). A note on large-scale motions in the tropics. *Journal of the Atmospheric Sciences*, *20*(6), 607–609. https://doi.org/10.1175/1520-0469(1963)020<0607:anolsm>2.0.co;2

Clapeyron, É. (1834). Mémoire sur la puissance motrice de la chaleur. *Journal de l'École polytechnique*, *14*, 153–190.

Copin, Y. (2012). Taylor diagram for python/matplotlib. *Zenodo*. https://doi.org/10.5281/zenodo.5548061

Couhert, A., Schneider, T., Li, J., Waliser, D. E., & Tompkins, A. M. (2010). The maintenance of the relative humidity of the subtropical free troposphere. *Journal of Climate*, *23*(2), 390–403. https://doi.org/10.1175/2009jcli2952.1

Eckart, C. (1960). *Hydrodynamics of atmospheres and oceans*. Pergamon Press.

Emanuel, K. A., Neelin, D. J., & Bretherton, C. S. (1994). On large-scale circulations in convecting atmospheres. *Quarterly Journal of the Royal Meteorological Society*, *120*(519), 1111–1143. https://doi.org/10.1256/smsqj.51901

Emanuel, K. A., Wing, A. A., & Vincent, E. M. (2014). Radiative-convective instability. *Journal of Advances in Modeling Earth Systems*, *6*(1), 75–90. https://doi.org/10.1002/2013ms000270

Fankhauser, J. C. (1969). Convective processes resolved by a mesoscale rawinsonde network. *Journal of Applied Meteorology*, *8*(5), 778–798. https://doi.org/10.1175/1520-0450(1969)008<0778:cprbam>2.0.co;2

Fildier, B., Muller, C., Pincus, R., & Fueglistaler, S. (2023). How moisture shapes low-level radiative cooling in subsidence regimes.

Forsythe, M. (2007). Atmospheric motion vectors: Past, present and future. In *ECMWF annual seminar* (pp. 1–79).

Fuchs-Stone, Ž., Raymond, D. J., & Sentić, S. (2020). OTREC2019: Convection over the East Pacific and southwest Caribbean. *Geophysical Research Letters*, *47*(11), e2020GL087564. https://doi.org/10.1029/2020gl087564

George, G., Stevens, B., Bony, S., Pincus, R., Fairall, C., Schulz, H., et al. (2021). JOANNE: Joint dropsonde observations of the atmosphere in tropical north Atlantic meso-scale environments [Dataset]. *Earth System Science Data*, *13*(11), 5253–5272. https://doi.org/10.5194/essd-13-5253-2021

George, G., Stevens, B., Bony, S., Vogel, R., & Naumann, A. K. (2023). Widespread shallow mesoscale circulations observed in the trades. *Nature Geoscience*, *16*(7), 1–6. https://doi.org/10.1038/s41561-023-01215-1

Gramazio, C. C., Laidlaw, D. H., & Schloss, K. B. (2017). Colorgorical: Creating discriminable and preferable color palettes for information visualization. *IEEE Transactions on Visualization and Computer Graphics*, *23*(1), 521–530. https://doi.org/10.1109/tvcg.2016.2598918

Hardman, M., James, D., & Goldsmith, P. (1972). The measurement of mesoscale vertical motions in the atmosphere. *Quarterly Journal of the Royal Meteorological Society*, *98*(415), 38–47. https://doi.org/10.1002/qj.49709841504

Hohenegger, C., Korn, P., Linardakis, L., Redler, R., Schnur, R., Adamidis, P., et al. (2022). Icon-sapphire: Simulating the components of the earth system and their interactions at kilometer and subkilometer scales. *Geoscientific Model Development Discussions*, *2022*, 1–42.
Hohenegger, C., & Stevens, B. (2013). Preconditioning deep convection with cumulus congestus. *Journal of the Atmospheric Sciences*, *70*(2), 448–464. https://doi.org/10.1175/jas-d-12-089.1
Holloway, C. E., Wing, A. A., Bony, S., Muller, C., Masunaga, H., L'Ecuyer, T. S., et al. (2017). Observing convective aggregation. *Surveys in Geophysics*, *38*(6), 1199–1236. https://doi.org/10.1007/s10712-017-9419-1
Holton, J. R., & Lindzen, R. S. (1968). A note on "Kelvin" waves in the atmosphere. *Monthly Weather Review*, *96*(6), 385–386. https://doi.org/10.1175/1520-0493(1968)096<0385:anokwi>2.0.co;2
Huaman, L., Schumacher, C., & Sobel, A. H. (2022). Assessing the vertical velocity of the east pacific ITCZ. *Geophysical Research Letters*, *49*(1), e2021GL096192. https://doi.org/10.1029/2021gl096192
Ingram, W. (2010). A very simple model for the water vapour feedback on climate change. *Quarterly Journal of the Royal Meteorological Society: A Journal of the Atmospheric Sciences, Applied Meteorology and Physical Oceanography*, *136*(646), 30–40. https://doi.org/10.1002/qj.546
Inoue, T. (1985). On the temperature and effective emissivity determination of semi-transparent cirrus clouds by bi-spectral measurements in the 10μm window region. *Journal of the Meteorological Society of Japan. Ser. II*, *63*(1), 88–99. https://doi.org/10.2151/jmsj1965.63.1_88
Jeevanjee, N., & Fueglistaler, S. (2020a). On the cooling-to-space approximation. *Journal of the Atmospheric Sciences*, *77*(2), 465–478. https://doi.org/10.1175/jas-d-18-0352.1
Jeevanjee, N., & Fueglistaler, S. (2020b). Simple spectral models for atmospheric radiative cooling. *Journal of the Atmospheric Sciences*, *77*(2), 479–497. https://doi.org/10.1175/jas-d-18-0347.1
Jeevanjee, N., Koll, D. D., & Lutsko, N. (2021). "Simpson's law" and the spectral cancellation of climate feedbacks. *Geophysical Research Letters*, *48*(14), e2021GL093699. https://doi.org/10.1029/2021gl093699
Jeyaratnam, J., Luo, Z. J., Giangrande, S. E., Wang, D., & Masunaga, H. (2021). A satellite-based estimate of convective vertical velocity and convective mass flux: Global survey and comparison with radar wind profiler observations. *Geophysical Research Letters*, *48*(1), e2020GL090675. https://doi.org/10.1029/2020gl090675
Kaplan, L. D. (1952). On the pressure dependence of radiative heat transfer in the atmosphere. *Journal of the Atmospheric Sciences*, *9*(1), 1–12. https://doi.org/10.1175/1520-0469(1952)009<0001:otpdor>2.0.co;2
Kiladis, G. N., Wheeler, M. C., Haertel, P. T., Straub, K. H., & Roundy, P. E. (2009). Convectively coupled equatorial waves. *Reviews of Geophysics*, *47*(2), RG2003. https://doi.org/10.1029/2008rg000266
Klocke, D., Brueck, M., Hohenegger, C., & Stevens, B. (2017). Rediscovery of the doldrums in storm-resolving simulations over the tropical Atlantic. *Nature Geoscience*, *10*(12), 891–896. https://doi.org/10.1038/s41561-017-0005-4
Konow, H., Ewald, F., George, G., Jacob, M., Klingebiel, M., Kölling, T., et al. (2021). EUREC^{4}A's HALO. *Earth System Science Data*, *13*(12), 5545–5563. https://doi.org/10.5194/essd-13-5545-2021
Lane, T. P., & Clark, T. L. (2002). Gravity waves generated by the dry convective boundary layer: Two-dimensional scale selection and boundary-layer feedback. *Quarterly Journal of the Royal Meteorological Society: A Journal of the Atmospheric Sciences, Applied Meteorology and Physical Oceanography*, *128*(583), 1543–1570. https://doi.org/10.1002/qj.200212858308
Lenschow, D. H., Krummel, P. B., & Siems, S. T. (1999). Measuring entrainment, divergence, and vorticity on the mesoscale from aircraft. *Journal of Atmospheric and Oceanic Technology*, *16*(10), 1384–1400. https://doi.org/10.1175/1520-0426(1999)016<1384:medavo>2.0.co;2
Liberzon, A., Käufer, T., Bauer, A., Vennemann, P., & Zimmer, E. (2021). *OpenPIV/openpiv-python: OpenPIV-Python v0.23.6*. Zenodo. https://doi.org/10.5281/zenodo.5009150
Lorentz, H. (1906). The absorption and emission lines of gaseous bodies. *Knaw, proceedings*, *8*, 1905–1906.
Madden, R. A., & Julian, P. R. (1971). Detection of a 40–50 day oscillation in the zonal wind in the tropical pacific. *Journal of the Atmospheric Sciences*, *28*(5), 702–708. https://doi.org/10.1175/1520-0469(1971)028<0702:doadoi>2.0.co;2
Mapes, B. E. (1993). Gregarious tropical convection. *Journal of the Atmospheric Sciences*, *50*(13), 2026–2037. https://doi.org/10.1175/1520-0469(1993)050<2026:gtc>2.0.co;2
Marc, O., Barret, M., Biancamaria, S., Dassas, K., Firmin, A., Gandois, L., et al. (2024). *Comprehensive carbon footprint of earth and environmental science laboratories: Implications for sustainable scientific practice*. ESS Open Archive.
Masunaga, H., & Luo, Z. J. (2016). Convective and large-scale mass flux profiles over tropical oceans determined from synergistic analysis of a suite of satellite observations. *Journal of Geophysical Research: Atmospheres*, *121*(13), 7958–7974. https://doi.org/10.1002/2016jd024753
Matsuno, T. (1966). Quasi-geostrophic motions in the equatorial area. *Journal of the Meteorological Society of Japan. Ser. II*, *44*(1), 25–43. https://doi.org/10.2151/jmsj1965.44.1_25
Montabone, L., Heavens, N., Alvarellos, J. L., Aye, M., Babuscia, A., Barba, N., et al. (2020). Observing Mars from areostationary orbit: Benefits and applications. In *Planetary science and astrobiology decadal survey 2023-2032*.
Morcrette, J.-J. (1991). Evaluation of model-generated cloudiness: Satellite-observed and model-generated diurnal variability of brightness temperature. *Monthly Weather Review*, *119*(5), 1205–1224. https://doi.org/10.1175/1520-0493(1991)119<1205:eomgcs>2.0.co;2
Muller, C., & Held, I. M. (2012). Detailed investigation of the self-aggregation of convection in cloud-resolving simulations. *Journal of the Atmospheric Sciences*, *69*(8), 2551–2565. https://doi.org/10.1175/jas-d-11-0257.1
Muller, C., Yang, D., Craig, G., Cronin, T., Fildier, B., Haerter, J. O., et al. (2022). Spontaneous aggregation of convective storms. *Annual Review of Fluid Mechanics*, *54*(1), 133–157. https://doi.org/10.1146/annurev-fluid-022421-011319
Narenpitak, P., Kazil, J., Yamaguchi, T., Quinn, P., & Feingold, G. (2021). From sugar to flowers: A transition of shallow cumulus organization during ATOMIC. *Journal of Advances in Modeling Earth Systems*, *13*(10), e2021MS002619. https://doi.org/10.1029/2021ms002619
Naumann, A. K., Stevens, B., & Hohenegger, C. (2019). A moist conceptual model for the boundary layer structure and radiatively driven shallow circulations in the trades. *Journal of the Atmospheric Sciences*, *76*(5), 1289–1306. https://doi.org/10.1175/jas-d-18-0226.1
Naumann, A. K., Stevens, B., Hohenegger, C., & Mellado, J. P. (2017). A conceptual model of a shallow circulation induced by prescribed low-level radiative cooling. *Journal of the Atmospheric Sciences*, *74*(10), 3129–3144. https://doi.org/10.1175/jas-d-17-0030.1
Nitta, T., & Esbensen, S. (1974). Heat and moisture budget analyses using BOMEX data. *Monthly Weather Review*, *102*(1), 17–28. https://doi.org/10.1175/1520-0493(1974)102<0017:hambau>2.0.co;2
Orlanski, I. (1975). A rational subdivision of scales for atmospheric processes. *Bulletin of the American Meteorological Society*, 527–530.
Paltridge, G. (1973). Direct measurement of water vapor absorption of solar radiation in the free atmosphere. *Journal of the Atmospheric Sciences*, *30*(1), 156–160. https://doi.org/10.1175/1520-0469(1973)030<0156:dmowva>2.0.co;2
Panofsky, H. (1946). Methods of computing vertical motion in the atmosphere. *Journal of Meteorology*, *3*(2), 45–49. https://doi.org/10.1175/1520-0469(1946)003<0045:mocvmi>2.0.co;2
Pascal, B. (1664). *Traités de l'équilibre des liqueurs, et de la pesanteur de la masse de l'air*. Savreux.

Peatman, S. C., Birch, C. E., Schwendike, J., Marsham, J. H., Dearden, C., Webster, S., et al. (2023). The role of density currents and gravity waves in the offshore propagation of convection over Sumatra. *Monthly Weather Review*, *151*(7), 1757–1777. https://doi.org/10.1175/mwr-d-22-0322.1

Poujol, B., & Bony, S. (2024). bpoujol/verticalvelocity: Version 1.0 [Software]. *Zenodo*. https://doi.org/10.5281/zenodo.12686667

Raymond, D., & Fuchs-Stone, Ž. (2021). Emergent properties of convection in OTREC and PREDICT. *Journal of Geophysical Research: Atmospheres*, *126*(4), e2020JD033585. https://doi.org/10.1029/2020jd033585

Rossby, C.-G. (1939). Relation between variations in the intensity of the zonal circulation of the atmosphere and the displacements of the semi-permanent centers of action. *Journal of Marine Research*, *2*(1), 38–55. https://doi.org/10.1357/002224039806649023

Salomonson, V. V., Barnes, W., Maymon, P. W., Montgomery, H. E., & Ostrow, H. (1989). MODIS: Advanced facility instrument for studies of the earth as a system [Dataset]. *IEEE Transactions on Geoscience and Remote Sensing*, *27*(2), 145–153. https://doi.org/10.1109/36.20292

Saunders, R., Hocking, J., Turner, E., Rayer, P., Rundle, D., Brunel, P., et al. (2018). An update on the RTTOV fast radiative transfer model (currently at version 12) [Software]. *Geoscientific Model Development*, *11*(7), 2717–2737. https://doi.org/10.5194/gmd-11-2717-2018

Savazzi, A. C. M., Nuijens, L., Sandu, I., George, G., & Bechtold, P. (2022). The representation of the trade winds in ECMWF forecasts and reanalyses during EUREC^{4}A. *Atmospheric Chemistry and Physics*, *22*(19), 13049–13066. https://doi.org/10.5194/acp-22-13049-2022

Schmetz, J., Pili, P., Tjemkes, S., Just, D., Kerkmann, J., Rota, S., & Ratier, A. (2002). An introduction to Meteosat second generation (MSG). *Bulletin of the American Meteorological Society*, *83*(7), 977–992. https://doi.org/10.1175/1520-0477(2002)083<0977:aitmsg>2.3.co;2

Schmit, T. J., Griffith, P., Gunshor, M. M., Daniels, J. M., Goodman, S. J., & Lebair, W. J. (2017). A closer look at the ABI on the goes-R series [Dataset]. *Bulletin of the American Meteorological Society*, *98*(4), 681–698. https://doi.org/10.1175/bams-d-15-00230.1

Schulz, H., Eastman, R., & Stevens, B. (2021). Characterization and evolution of organized shallow convection in the downstream North Atlantic trades. *Journal of Geophysical Research: Atmospheres*, *126*(17), e2021JD034575. https://doi.org/10.1029/2021jd034575

Schulz, H., & Stevens, B. (2018). Observing the tropical atmosphere in moisture space. *Journal of the Atmospheric Sciences*, *75*(10), 3313–3330. https://doi.org/10.1175/jas-d-17-0375.1

Soden, B. J. (1998). Tracking upper tropospheric water vapor radiances: A satellite perspective. *Journal of Geophysical Research*, *103*(D14), 17069–17081. https://doi.org/10.1029/98jd01151

Soden, B. J., & Bretherton, F. P. (1993). Upper tropospheric relative humidity from the GOES 6.7 μm channel: Method and climatology for July 1987. *Journal of Geophysical Research*, *98*(D9), 16669–16688. https://doi.org/10.1029/93jd01283

Stephan, C. C., Lane, T., & Jakob, C. (2020). Gravity wave influences on mesoscale divergence: An observational case study. *Geophysical Research Letters*, *47*(1), e2019GL086539. https://doi.org/10.1029/2019gl086539

Stephan, C. C., Schnitt, S., Schulz, H., Bellenger, H., De Szoeke, S. P., Acquistapace, C., et al. (2021). Ship-and island-based atmospheric soundings from the 2020 EUREC^{4}A field campaign [Dataset]. *Earth System Science Data*, *13*(2), 491–514. https://doi.org/10.5194/essd-13-491-2021

Stevens, B., Bony, S., Brogniez, H., Hentgen, L., Hohenegger, C., Kiemle, C., et al. (2020). Sugar, gravel, fish and flowers: Mesoscale cloud patterns in the trade winds. *Quarterly Journal of the Royal Meteorological Society*, *146*(726), 141–152. https://doi.org/10.1002/qj.3662

Stevens, B., Bony, S., Farrell, D., Ament, F., Blyth, A., Fairall, C., et al. (2021). EUREC^{4}A. *Earth System Science Data*, *13*(8), 4067–4119.

Stevens, B., Satoh, M., Auger, L., Biercamp, J., Bretherton, C. S., Chen, X., et al. (2019). DYAMOND: The dynamics of the atmospheric general circulation modeled on non-hydrostatic domains. *Progress in Earth and Planetary Science*, *6*(1), 1–17. https://doi.org/10.1186/s40645-019-0304-z

Straus, D., & Paolino, D. (2008). Intermediate time error growth and predictability: Tropics versus mid-latitudes. *Tellus A: Dynamic Meteorology and Oceanography*, *61*(5), 579–586. https://doi.org/10.1111/j.1600-0870.2009.00411.x

Takayabu, Y. N. (1994). Large-scale cloud disturbances associated with equatorial waves part I: Spectral features of the cloud disturbances. *Journal of the Meteorological Society of Japan. Ser. II*, *72*(3), 433–449. https://doi.org/10.2151/jmsj1965.72.3_433

Taylor, K. E. (2001). Summarizing multiple aspects of model performance in a single diagram. *Journal of Geophysical Research*, *106*(D7), 7183–7192. https://doi.org/10.1029/2000jd900719

Touzé-Peiffer, L., Vogel, R., & Rochetin, N. (2022). Cold pools observed during EUREC4A: Detection and characterization from atmospheric soundings. *Journal of Applied Meteorology and Climatology*, *61*(5), 593–610. https://doi.org/10.1175/jamc-d-21-0048.1

Uma, K. N., Das, S. S., Ratnam, M. V., & Suneeth, K. V. (2021). Assessment of vertical air motion among reanalyses and qualitative comparison with very-high-frequency radar measurements over two tropical stations. *Atmospheric Chemistry and Physics*, *21*(3), 2083–2103. https://doi.org/10.5194/acp-21-2083-2021

van den Heever, S., Haddad, Z., Tanelli, S., Stephens, G., Posselt, D., Kim, Y., et al. (2022). The INCUS mission. In *Egu general assembly conference abstracts* (p. EGU22-9021).

Vogel, R., Albright, A. L., Vial, J., George, G., Stevens, B., & Bony, S. (2022). Strong cloud–circulation coupling explains weak trade cumulus feedback. *Nature*, *612*(7941), 1–5. https://doi.org/10.1038/s41586-022-05364-y

Vömel, H., Goodstein, M., Tudor, L., Witte, J., Fuchs-Stone, Ž., Sentić, S., et al. (2021). High-resolution in situ observations of atmospheric thermodynamics using dropsondes during the organization of tropical East Pacific convection (OTREC) field campaign. *Earth System Science Data*, *13*(3), 1107–1117. https://doi.org/10.5194/essd-13-1107-2021

Wang, J., Bian, J., Brown, W. O., Cole, H., Grubišić, V., & Young, K. (2009). Vertical air motion from T-REX radiosonde and dropsonde data. *Journal of Atmospheric and Oceanic Technology*, *26*(5), 928–942. https://doi.org/10.1175/2008jtecha1240.1

Wheeler, M., & Kiladis, G. N. (1999). Convectively coupled equatorial waves: Analysis of clouds and temperature in the wavenumber–frequency domain. *Journal of the Atmospheric Sciences*, *56*(3), 374–399. https://doi.org/10.1175/1520-0469(1999)056<0374:ccewao>2.0.co;2

Wing, A. A., & Emanuel, K. A. (2014). Physical mechanisms controlling self-aggregation of convection in idealized numerical modeling simulations. *Journal of Advances in Modeling Earth Systems*, *6*(1), 59–74. https://doi.org/10.1002/2013ms000269

Wing, A. A., Emanuel, K. A., Holloway, C. E., & Muller, C. (2018). Convective self-aggregation in numerical simulations: A review. Shallow clouds, water vapor, circulation, and climate sensitivity (pp. 1–25).

Yang, D. (2021). A shallow-water model for convective self-aggregation. *Journal of the Atmospheric Sciences*, *78*(2), 571–582. https://doi.org/10.1175/jas-d-20-0031.1

Yu, F., Wu, X., Yoo, H., Qian, H., Shao, X., Wang, Z., & Iacovazzi, R. (2021). Radiometric calibration accuracy and stability of GOES-16 ABI infrared radiance. *Journal of Applied Remote Sensing*, *15*(4), 048504. https://doi.org/10.1117/1.jrs.15.048504

Zhang, J., Chen, H., Zhu, Y., Shi, H., Zheng, Y., Xia, X., et al. (2019). A novel method for estimating the vertical velocity of air with a descending radiosonde system. *Remote Sensing*, *11*(13), 1538. https://doi.org/10.3390/rs11131538

References From the Supporting Information

Chou, M.-D. (1986). Atmospheric solar heating rate in the water vapor bands. *Journal of Applied Meteorology and Climatology*, *25*(11), 1532–1542. https://doi.org/10.1175/1520-0450(1986)025<1532:ashrit>2.0.co;2

Clausius, R. (1850). Über die bewegende Kraft der Wärme und die Gesetze, welche sich daraus für die Wärmelehre selbst ableiten lassen. *Annalen der Physik*, *155*(3), 368–397. https://doi.org/10.1002/andp.18501550306

Masunaga, H., L'Ecuyer, T. S., & Kummerow, C. D. (2006). The Madden–Julian oscillation recorded in early observations from the tropical rainfall measuring mission (TRMM). *Journal of the Atmospheric Sciences*, *63*(11), 2777–2794. https://doi.org/10.1175/jas3783.1

Munteanu, C., Negrea, C., Echim, M., & Mursula, K. (2016). Effect of data gaps: Comparison of different spectral analysis methods. *Annales Geophysicae*, *34*(4), 437–449. https://doi.org/10.5194/angeo-34-437-2016

NOAA. (2020). NOAA solar calculator. Retrieved from https://gml.noaa.gov/grad/solcalc/solareqns.PDF

Segelstein, D. J. (1981). *The complex refractive index of water (Unpublished doctoral dissertation)*. University of Missouri–Kansas City.

Vidot, J., Baran, A. J., & Brunel, P. (2015). A new ice cloud parameterization for infrared radiative transfer simulation of cloudy radiances: Evaluation and optimization with IIR observations and ice cloud profile retrieval products. *Journal of Geophysical Research: Atmospheres*, *120*(14), 6937–6951. https://doi.org/10.1002/2015jd023462